

1 Mitigation of bias sources for atmospheric temperature and 2 humidity in the mobile Weather & Aerosol Raman Lidar 3 (WALI)

4 **Julien Totems, Patrick Chazette and Alexandre Baron**

5 [1]{Laboratoire des Sciences du Climat et de l'Environnement, CEA, Gif-sur-Yvette, France}

6 Correspondence to: J. Totems (julien.totems@cea.fr)

7 **Abstract**

8 Lidars using vibrational and rotational Raman scattering to continuously monitor both the water
9 vapor and temperature profiles in the low and middle troposphere offer enticing perspectives
10 for applications in weather prediction and studies of aerosol/cloud/water vapor interactions by
11 deriving simultaneously relative humidity and atmospheric optical properties. Several heavy
12 systems exist in European laboratories but only recently have they been downsized and
13 ruggedized for deployment in the field. In this paper, we describe in detail the technical choices
14 made during the design and calibration of the new Raman channels for the mobile Weather and
15 Aerosol Lidar (WALI), going over the important sources of bias and uncertainty on the water
16 vapor & temperature profiles stemming from the different optical elements of the instrument.
17 For the first time, the impacts of interference filters and non-common-path differences between
18 Raman channels, and their mitigation, are particularly investigated, using horizontal shots in a
19 homogeneous atmosphere. For temperature, the magnitude of the highlighted biases can be
20 much larger than the targeted absolute accuracy of 1°C defined by the WMO (up to 6°C bias
21 below 300 m range). Measurement errors are quantified using simulations and a number of
22 radiosoundings launched close to the laboratory. After de-biasing, the remaining mean
23 differences are below 0.1 g/kg on water vapor, 1°C on temperature, and RMS differences are
24 consistent with the expected error from lidar noise, calibration uncertainty, and horizontal
25 inhomogeneities of the atmosphere between the lidar and radiosondes.

26 **1 Introduction**

27 Atmospheric temperature and humidity in the low atmosphere are together essential to
28 comprehend weather phenomena and their evolution in a changing climate. Through the effect
29 of relative humidity on aerosol hygroscopicity and cloud formation, they also influence the

30 radiative balance of the Earth, generating the largest uncertainties in climate projections (IPCC,
31 2013). For both weather and climate prediction, observation means have evolved tremendously,
32 notably with satellite retrievals of moisture and temperature routinely assimilated in numerical
33 models. Yet remote sensing techniques from spaceborne missions have difficulties probing the
34 lower troposphere below 2-3 km in altitude, and have vertical resolutions that are too low,
35 greater than 1 km in the lower troposphere (e.g. Prunet et al., 1998; Crevoisier et al., 2014).
36 They are thus unable to resolve temperature inversions and thin dry/humid air masses (e.g.
37 Chazette et al., 2014; Hammann et al., 2015; Totems et al., 2019). Providing complementary
38 profiles of the important thermodynamic variables in the first kilometres of the atmosphere,
39 where most of the water vapour and temperature vertical variability is confined, is of paramount
40 importance for both weather forecast and reducing aerosol-induced uncertainty on climate
41 models (Wulfmeyer et al., 2015).

42 Given their capacity for continuous, well-resolved and precise temperature measurements in
43 the lower troposphere, Vibrational Raman (VR) and Rotational Raman (RR) lidars have
44 emerged as adequate tools in this endeavour. Water vapor profilers are now well-established
45 (from Whiteman et al., 1992 to e.g. Dinoev et al., 2013), whereas temperature profilers have
46 recently become more widespread and powerful (from Cooney, 1972 and Vaughan et al., 1993
47 to e.g. Weng et al., 2018 or Martucci et al., 2021). Without tackling turbulence-scale resolution
48 which is the prerogative of heavier systems like the Raman lidars of the University of
49 Hohenheim (Behrendt et al., 2015), the University of Basilicata (Di Girolamo et al., 2017) or
50 ARTHUS (Atmospheric Raman Temperature and Humidity Sounder, Lange et al., 2019), there
51 is a need for field-deployable instruments capable of fulfilling the breakthrough requirements
52 set by the World Meteorological Organization in terms of accuracy on atmospheric temperature
53 and humidity in the low troposphere (WMO, 2017). Lidar profiles have proven beneficial for
54 both numerical weather prediction (NWP) models (e.g. Adam et al., 2016; Fourrié et al., 2019),
55 the study of dynamic processes in the planetary boundary layer (PBL) (e.g. Behrendt et al.,
56 2015) or interactions between water vapor and aerosols (e.g. Navas-Guzmán et al., 2019). But
57 to obtain the absolute accuracies demanded here, especially that of 1°C or less on temperature,
58 the required accuracy on the lidar channel ratios and their calibration is extremely stringent,
59 and the sources of systematic error seldom discussed in the literature (Behrendt and Reichardt,
60 2000; Simeonov et al., 1999; Whiteman et al., 2012).

61 Within the European lidar landscape, WALI (Weather and Aerosol Lidar) is a seasoned mobile
62 Rayleigh-Mie-Raman system, “eyesafe” at 355 nm, first deployed during the HyMeX
63 international field campaign and subsequently ChArMEx and PARCS, for aerosol and water

64 vapor profiling (resp. Hydrological cycle in the Mediterranean eXperiment, Chemistry and
65 Aerosol in the Mediterranean Experiment, Pollution in the Arctic System; Chazette et al.,
66 2014b, 2018; Totems et al., 2019; Totems and Chazette, 2016). In its latest evolution, the VR
67 channels have been replaced by a Newton reflector and a polychromator also including RR
68 channels for temperature profiling. On this occasion, we have established that biases due to
69 various sources, in particular from the dependency of spectral filtering on the angle of
70 incidence, detector non-uniformities and other non-common-path differences between Raman
71 channels, may be several times greater than the requirements if left unchecked. Correctible as
72 they are by measuring the ratios of overlap factors on the individual channels, these effects are
73 not reported in the literature of lidar temperature measurements. However, they were bound to
74 appear given the physical characteristics of the systems mentioned hereabove.

75 The aims of this paper are: i) to compile for the first time the sources of systematic error that
76 must be considered and mitigated when using a Raman lidar to profile atmospheric temperature
77 and humidity, ii) to validate WALI as a dependable profiler deployable for field campaigns,
78 satisfying the requirements set by the WMO.

79 The theory of the Raman lidar retrieval of the atmospheric temperature and WVMR, the error
80 budget on these parameters, and the known causes of bias are recalled in section 2, as well as
81 the principle and limitations of the overlap measurement method. In section 3, after
82 summarizing the characteristics of WALI, we propose a sequential review of the components
83 of the lidar chain, characterizing and mitigating the error sources. The results of a calibration
84 and qualification experiment using radiosondes follow in section 4. A conclusion and outlooks
85 are presented in section 5.

86 **2 Theoretical considerations**

87 **2.1 Raman lidar retrieval of humidity and temperature**

88 We will introduce notations by briefly recalling the theory of the retrieval of water vapor content
89 and temperature by the Raman lidar technique; the complete theory has been extensively
90 derived before, by Whiteman et al. (1992) and Behrendt (2005) respectively, among others.

91 The vertical profiles of water vapor mixing ratio (WVMR) r_{H_2O} and temperature T are
92 calculated from the ratios of the H₂O / N₂-vibrational Raman (VR) channels and the RR2 (high-
93 J number) / RR1 (low-J number) rotational Raman (RR) channels, respectively:

$$R(z) = \frac{S_{H_2O}(z)}{S_{N_2}(z)} \quad (1)$$

$$Q(z) = \frac{S_{RR2}(z)}{S_{RR1}(z)} \quad (2)$$

94 Signals $S_j(z)$ of Raman channels j have all been previously averaged over the required altitude
 95 and time to improve the signal to noise ratio (SNR), and corrected for i) electronic baseline
 96 variations by subtracting a baseline recorded every few profiles with detector (photomultiplier
 97 tube, PMT) gain set to zero, ii) the sky background mean value assessed on pre-trigger or post-
 98 signal samples, iii) PMT gain variations (allowed on the VR channels to optimize daytime
 99 dynamic range, eg. Chazette et al. (2014b)), iv) known leakage of the elastic return in the RR
 100 filters (Behrendt and Reichardt, 2000). $S_j(z)$ are thus expressed as:

$$S_j(z) = \frac{1}{G_j(U_j)} (S_{j,raw}(z) - \hat{L}_j(z) - \hat{B}_j) - \hat{\epsilon}_j S_{elas}(z) \quad (3)$$

101 where G_j is the channel gain controlled by PMT voltage U_j , $S_{j,raw}$ is the raw lidar signal, \hat{L}_j is
 102 the estimated baseline, \hat{B}_j is the estimated sky background parasitic signal, $\hat{\epsilon}_j$ is the estimated
 103 residual transmittance of the emitted laser wavelength through the interference filter (IF) of
 104 Raman channel j compared to the elastic channel, and S_{elas} is the elastic signal. \hat{x} denotes the
 105 estimate of x .

106 Both R and Q must then also be corrected for the difference of atmospheric transmission
 107 between the two Raman channels and the ratio of overlap factors:

$$R'(z) = \frac{\exp(\Delta\tau(z))}{\widehat{OR}_R(z)} R(z) \quad (4)$$

$$Q'(z) = \frac{1}{\widehat{OR}_Q(z)} Q(z) \quad (5)$$

108 where $\Delta\tau(z)$ is the difference of optical thickness from the lidar until range z observed between
 109 the wavelengths of the two VR channels, and where $\widehat{OR}_R(z)$ and $\widehat{OR}_Q(z)$ are the estimated
 110 ratios of the overlap factors of the two VR / RR channels respectively (expressed in section
 111 2.4). With an emitted wavelength at 355 nm, $\Delta\tau(z)$ between 387 and 407 nm seldom produces
 112 deviations above 5%, and can be efficiently estimated using an average atmospheric density
 113 profile for molecular optical thickness and the N₂-Raman channel itself for aerosol optical
 114 thickness (e.g. Whiteman, 2003).

115 The WVMR is simply proportional to the VR scattering ratio between H₂O and N₂, since
 116 nitrogen gas has a constant mixing ratio in the troposphere and stratosphere. The temperature
 117 is retrieved from the more complex dependency of the RR scattering cross sections between the
 118 two channels RR1 and RR2. The respective estimates \hat{r}_{H_2O} and \hat{T} (to be distinguished from the
 119 true values without ^) are obtained, after calibration, by:

$$\hat{r}_{H_2O}(z) = \hat{K}R'(z) \quad (6)$$

$$\hat{T}(z) = \hat{f}^{-1}(Q'(z)) \quad (7)$$

120 where \hat{K} is the estimate of the calibration coefficient for WVMR combining all instrumental
 121 constants. Calibration function \hat{f} is the estimate of the temperature dependency of the ratio of
 122 RR cross-sections. It takes into account the instrumental constants of the two RR channels. We
 123 take the model previously selected for operational purposes by Behrendt (2005):

$$Q' = f(T) = \exp\left(a + \frac{b}{T} + \frac{c}{T^2}\right) \quad (8)$$

124 with a, b, c the coefficients of a polynomial regression of $\ln(Q')$ as a function of $1/T$. \hat{K} and \hat{f}
 125 are obtained by confronting lidar profiles of R' and Q' with collocated in-situ measurements of
 126 r_{H_2O} and T (e.g. from a radiosounding), aiming for a wide range of values for a better constraint
 127 on the calibration.

128 2.2 Simple error budget

129 In this section, we will make a first assessment of the acceptable error on R and Q starting from
 130 the accuracy requirements for WVMR and temperature profiles, which ensue from each
 131 scientific need, as compiled by Wulfmeyer et al. (2015) for key applications. Monitoring,
 132 verification (e.g. model qualification or calibration/validation of satellites) and data
 133 assimilation purposes can be adequately addressed by a profiler capable of i) <5% noise error
 134 and <2-5% bias for water vapor, ii) <1°C noise error and <0.2-0.5°C bias for temperature. In a
 135 simple error budget, we can use requirements of $\left(\frac{\Delta r_{H_2O}}{r_{H_2O}}\right)_{max} = 5\%$ for WVMR, and
 136 $\Delta T_{max} = 1^\circ\text{C}$ for temperature, to give a first idea of the different expectations for the
 137 performance of a VR/RR lidar.

138 Eqs. (4-8) allow to derive constraints on the acceptable relative error on the corrected lidar
 139 observables R' and Q' , for either random noise or bias, as:

$$\left(\frac{\Delta R'}{R'}\right)_{max} = \left(\frac{\Delta r_{H_2O}}{r_{H_2O}}\right)_{max} \quad (9)$$

$$\left(\frac{\Delta Q'}{Q'}\right)_{max} = \frac{dQ'/dT}{Q'} \Delta T_{max} \quad (10)$$

140 The relative error on R is equal to the constraint on WVMR, i.e. 5%. An assessment of the
 141 relative error on Q is performed considering the RR filter parameters given in Table 2 (section
 142 3) to yield the following numerical application: around $T_0 = 0^\circ\text{C}$, $Q'(T_0) = 0.44$ and $dQ'/dT(T_0)$
 143 $= +0.35/100^\circ\text{C}$, so that: $\left(\frac{\Delta Q'}{Q'}\right)_{max} = 0.79\% \Delta T_{max} (^\circ\text{C})$.

144 Table 1. Summary of accuracy requirements from Wulfmeyer et al. (2015) and corresponding
 145 constraints on ratios R' and Q' . Resulting errors on relative humidity RH at 0°C and 50%RH.

Parameter	Random error	Systematic error (bias)
r_{H_2O}	<5% relative	<2-5% relative
T	<1°C	<0.2-0.5°C
R'	<5% i.e. $SNR > 20$	<2-5%
Q'	<0.8% at 0°C i.e. $SNR > 125$	<0.12-0.4% at 0°C
RH	4.3%RH at $T = 0^\circ\text{C}$, $RH = 50\%$	1.2-2.9%RH at $T = 0^\circ\text{C}$, $RH = 50\%$

146

147 The results, summarized in Table 1, have very important implications. In order to fulfill WMO
 148 requirements for temperature and WVMR measurements, the Q' ratio must be 6-10 times more
 149 accurate than R' . However, Raman cross-sections are larger for the RR channels than for the
 150 H_2O VR channel. Hence when dealing with a RR+VR lidar rather than a VR system, the main
 151 difficulties are not only due to low signal-to-noise ratio but also encompass strong constraints
 152 linked to instrumental biases. SNR as used in Table 1 is defined on R and Q at the final
 153 resolution, and is calculated from the individual signal variances and means (including laser &
 154 sky-background photon noise, detection noise), as:

$$SNR_R = \left(\frac{\text{var}(S_{N_2})}{\langle S_{N_2} \rangle^2} + \frac{\text{var}(S_{H_2O})}{\langle S_{H_2O} \rangle^2} \right)^{-\frac{1}{2}} \quad (11)$$

$$SNR_Q = \left(\frac{\text{var}(S_{RR1})}{\langle S_{RR1} \rangle^2} + \frac{\text{var}(S_{RR2})}{\langle S_{RR2} \rangle^2} \right)^{-\frac{1}{2}} \quad (12)$$

155 SNR_R , typically limited by the H₂O channel, must be above ~20 and SNR_Q must be above ~125
 156 to satisfy the requirements given above. Such high values can be reached by increasing the laser
 157 power and pulse repetition frequency (PRF), or enlarging the integration over altitude and time,
 158 as SNR is usually magnified by the square roots of the energy and number of averaged samples.
 159 However, limits on the latter are also set by Wulfmeyer et al. (2015) for the same applications;
 160 integration range Δz should be below 100 m in the PBL and 300 m in the lower free troposphere,
 161 whereas an integration time Δt between 15 (assimilation and verification) and 60 min
 162 (monitoring) is required.

163 We derive the errors expected on RH given those on temperature and WVMR at the bottom of
 164 Table 1. Here and in the following, %RH denote absolute percentage units on RH, whereas %
 165 denote relative errors. Relative humidity is derived as a function of atmospheric pressure,
 166 temperature and WVMR, using standard empirical relationships for the water vapor saturation
 167 pressure. Here, we use the Buck equation (Buck, 1981), which is accurate within 0.2% between
 168 -40°C and $+100^\circ\text{C}$:

$$P_{wv,sat} = 6.1121 \frac{T}{T + 257.14^\circ\text{C}} \exp\left(18.678 - \frac{T}{T + 234.5^\circ\text{C}}\right) \quad (13)$$

$$RH = \frac{P}{P_{wv,sat}} \frac{r_{H_2O}}{r_{H_2O} + 621.991 \text{ g kg}^{-1}} \quad (14)$$

169 with P pressure and $P_{wv,sat}$ the water vapor saturation pressure in hPa, T temperature in $^\circ\text{C}$.

170 2.3 Sources of bias

171 Biases arising from inaccurate measurement of any of the estimated factors of Eqs. (3-7), or
 172 from a variation after that measurement due to instabilities in the instrument, must also be
 173 smaller than the aforementioned values of 2-5% for WVMR and 0.12-0.4% for temperature,
 174 the latter being especially difficult to reach. Their impact must be mitigated either by careful
 175 design or by precise estimation.

176 The expected (i.e. noiseless) values of R and Q can be detailed as:

$$\overline{R(z)} = \frac{O_{H_2O}(z)}{O_{N_2}(z)} \frac{K_{H_2O}}{K_{N_2}} \frac{\sigma_{H_2O}}{\sigma_{N_2}} r_{H_2O}(z) \quad (15)$$

$$\overline{Q(z)} = \frac{O_{RR2}(z) K_2 \sigma_{RR2}(T(z))}{O_{RR1}(z) K_1 \sigma_{RR1}(T(z))} \quad (16)$$

177 with \bar{x} denoting the expected value of variable x , K_j , σ_j and $O_j(z)$, the instrumental constant,
 178 Raman backscatter cross-section, and overlap factor of channel j , respectively. To simplify our
 179 discussion, we choose to incorporate any deviation that affects the ratios without a range-
 180 dependence into the instrumental constant ratio, and any deviation with a range-dependence
 181 into the overlap ratio.

182 As previously explained, the impact of deviations on variables in Eq. (15) remains tolerable
 183 below a few percent, but for the distinctly more constrained temperature retrieval, the variables
 184 in Eq. (16) are affected by the following effects that directly induce significant bias:

- 185 • Laser wavelength drift or filter central wavelength (CWL) drift with temperature both
 186 affect the ratios indiscriminately with range. By simulating the variation of Q with the
 187 WALI filter parameters (section 3), we find a large impact of a wavelength drift $\Delta\lambda$
 188 (measured between the laser on one side and both interference filters on the other side):
 189 $dQ/Q/d\lambda \approx -0.26 \text{ pm}^{-1}$ and $\Delta T \approx -0.34^\circ\text{C pm}^{-1} \Delta\lambda$, meaning just 3 pm drift in
 190 either filter or laser wavelengths can lead to biases above 1°C . That is one of the reasons
 191 why the laser must be frequency-stabilized. Also, IFs subjected to fluctuations of local
 192 temperature are known to experience CWL drifts; for WALI's filters manufactured by
 193 Materion, this amounts to $1.28 \text{ pm } ^\circ\text{C}^{-1}$ (value given by the manufacturer after their
 194 material dilation simulation). The temperature of the polychromator must thus be kept
 195 stable within 1°C for this bias to become negligible.
- 196 • Filter CWL variation with angle of incidence (AOI) on the IF generates a channel
 197 transmittance variation which is range-dependent, and different for each filter. Indeed,
 198 this variation ΔCWL is approached by (e.g. Hayden Smith and Smith, 1990):

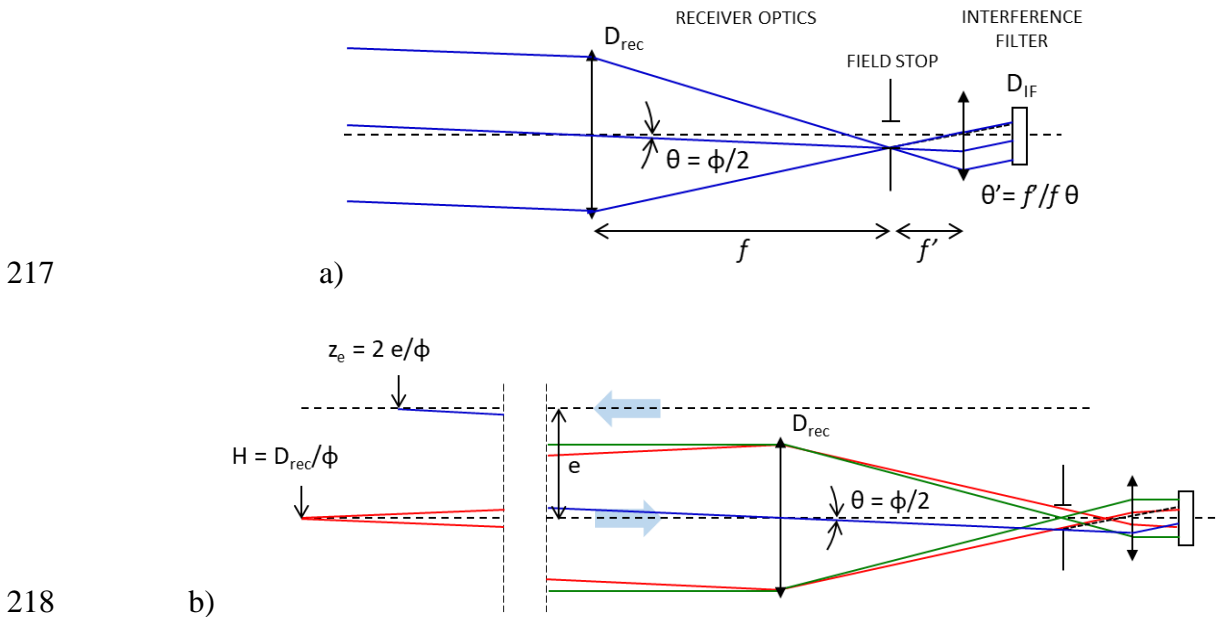
$$\Delta\text{CWL}(\theta') \approx \text{CWL} \frac{\theta'^2}{2n_{eff}^2} \quad (17)$$

199 where CWL is the filter central wavelength, θ' is the angle of incidence on the filter
 200 (assumed small), and n_{eff} is the effective refractive index of the filter. For the RR1 filter
 201 ($n_{eff} = 1.62$), we obtain as much as $\Delta\text{CWL}(\theta') \approx 43 \text{ pm } \theta'(^{\circ})^2$. The problem stems from
 202 the fact that because the filter is in the pupil plane, after collimation of the received
 203 beam, each angle of incidence corresponds to a different point in the focal plane of the

204 receiver, which in turns corresponds to a field angle θ of the lidar, as seen on Figure 1
 205 a). Aperture number conservation across the receiving optical system imposes

$$\theta' = \frac{f}{f'} \theta > \frac{D_{rec}}{D_{IF}} \theta \quad (18)$$

206 where f and f' are the receiver/recollimation focal lengths, D_{rec} and D_{IF} are the receiver
 207 and IF diameters. For a 150-mm diameter receiver using a 1-inch diameter (22 mm clear
 208 aperture) IF, we obtain at least $\theta' = 0.39^\circ$ for a $\theta = 1$ mrad field angle, producing
 209 $\Delta CWL(\theta') \approx 6.6$ pm and already $\Delta T \approx 2,2^\circ\text{C}$. Note that the impact gets
 210 proportionately larger with the diameter of the receiver. Because the optical path of each
 211 channel is independently aligned, this always induces different overlap factors even
 212 when sharing the same telescope. This large effect must be calibrated and corrected, yet
 213 its impact was never discussed before in the RR lidar literature, despite being three times
 214 as large in other systems with 450 mm receivers. This impact can be mitigated by
 215 attacking the filters at normal incidence, where the derivative of CWL as a function of
 216 AOI (see Eq. (17)) is minimal.



219 Figure 1. a) Definition of useful parameters for field angle θ and filter angle of incidence
 220 θ' calculations. f : receiver focal length, D_{rec} : receiver diameter, ϕ : full lidar field-of-
 221 view, f' : collimation focal length, D_{IF} : IF diameter. b) Definition of metrics for overlap
 222 calculations. e : emitter-receiver separation, H : hyperfocal distance, z_e : entry distance of
 223 laser into field-of-view. Green/red/blue lines represent rays from infinity/finite
 224 distance/offset emitted beam, respectively.

- 225 • Detector response non-uniformity up to $\pm 12\%$, both as a function of impact point on the
226 active surface and of angle of incidence, is now specified on the cathodes of PMTs used
227 at 400 nm wavelength (Hamamatsu (2007), Section 4.3.3). The amplitude was found to
228 be much larger by Simeonov et al. (1999), with significant impact. This effect has been
229 bluntly limited in all our lidars by putting the cathode plane as far as possible before the
230 focal plane, while still avoiding vignetting. It can still be responsible for differences of
231 overlap factors between channels.
- 232 • Uncalibrated PMT gain or digitizer baseline variations will of course induce bias in the
233 channel system constants. We will see how to mitigate these effects.
- 234 • Slight variations of overlap or channel transmittance after calibration will be directly
235 responsible for bias. In the next sub-section, we discuss how they can appear.

236 2.4 Overlap measurement with horizontal shots and limitations

237 Range-dependent biases influence the lower part of the lidar profiles exactly like the overlap
238 factors. They significantly impact the profiles up to a given range from the emitter, depending
239 on the characteristics of the receiving optics as seen above, but also on the quality of the
240 alignments, which is seldom twice the same. Two methods are used in the literature to
241 approximate the actual overlap factors of a Raman lidar: i) an iterative Klett inversion of elastic
242 and Raman channels sharing the same telescope is easy to achieve (Wandinger and Ansmann,
243 2002) but inefficient when non-common path errors are involved, whereas ii) the method of
244 aiming the lidar horizontally (e.g. Sicard et al., 2002; Chazette and Totems, 2017) is sometimes
245 impractical but more direct and yields more accurate results in an horizontally homogeneous
246 atmosphere over a range of 1 to 2 km. In the context of RR measurements, it is necessary to
247 implement the latter, and also to measure the ratios of overlap factors, rather than the overlap
248 factors themselves, thus avoiding errors due to an imprecise estimation of atmospheric
249 extinction.

250 Considering a horizontal line of sight in a supposedly homogeneous atmosphere, the expected
251 values of ratios R and Q can be expressed as:

$$\overline{R(z)} = R(z_\infty) \frac{O_{H_2O}(z)}{O_{N_2}(z)} \exp(-\Delta\alpha \cdot z) \quad (19)$$

$$\overline{Q(z)} = Q(z_\infty) \frac{O_{RR2}(z)}{O_{RR1}(z)} \quad (20)$$

252 where $R(z_\infty)$ and $Q(z_\infty)$ are the values observed when all overlap factors have become constant
 253 at a sufficiently large range from the lidar, noted z_∞ , after which variations of the optical path
 254 inside the reception channels become negligible. $\Delta\alpha = \alpha(407\text{nm}) - \alpha(387\text{nm})$ is the difference
 255 of atmospheric extinction between the two VR wavelengths.

256 To evaluate z_∞ , we introduce in Figure 1 b) parameters that characterize the overlap of a paraxial
 257 or coaxial lidar (e.g. Kuze et al., 1998): i) $z_e = 2e/\phi$ at which the emitted laser beam located at
 258 distance e from the receiver axis enters the field of view, whose full size is ϕ ; z_e is null for a
 259 coaxial system ii) $H = D_{rec}/\phi$, the so-called hyperfocal distance, minimum range from which
 260 the beam originating from a point still fully enters the field stop; iii) $H_{IF} = 2D_{rec}f/f'\theta'_{max}$, that
 261 we might call the filter hyperfocal distance, similarly to the former, the minimum range from
 262 which the image of a point does not exceed θ'_{max} , the AOI on the IF that significantly changes
 263 its transmittance. z_∞ is above the maximum of those three, which is usually H_{IF} . If we use for
 264 θ'_{max} the AOI value causing 1°C bias on temperature per Eq. (10) and Eq. (15), we find: $z_\infty > H_{IF}$
 265 $= 780$ m. Note that z_∞ can reach several km with misaligned filters.

266 If for instance the lidar can be mounted on a rotating platform capable of aiming horizontally,
 267 the overlap ratios $OR_R(z) = O_{H2O}(z)/O_{N2}(z)$ and $OR_Q(z) = O_{RR2}(z)/O_{RR1}(z)$ can be
 268 estimated with suitable precision ($\sim 10^{-3}$) by averaging the signals over time and smoothing them
 269 over range, and finally correcting for differential of extinction on the VR ratio:

$$\widehat{OR_R}(z) = \frac{R(z)}{R(z_\infty)} \exp(\Delta\alpha \cdot z) \quad (21)$$

$$\widehat{OR_Q}(z) = \frac{Q(z)}{Q(z_\infty)} \quad (22)$$

270 These estimates of the overlap ratios will then be used during signal processing for vertical
 271 shots as in Eq. (4) and (5). However, assumptions are made for the former estimation, namely:

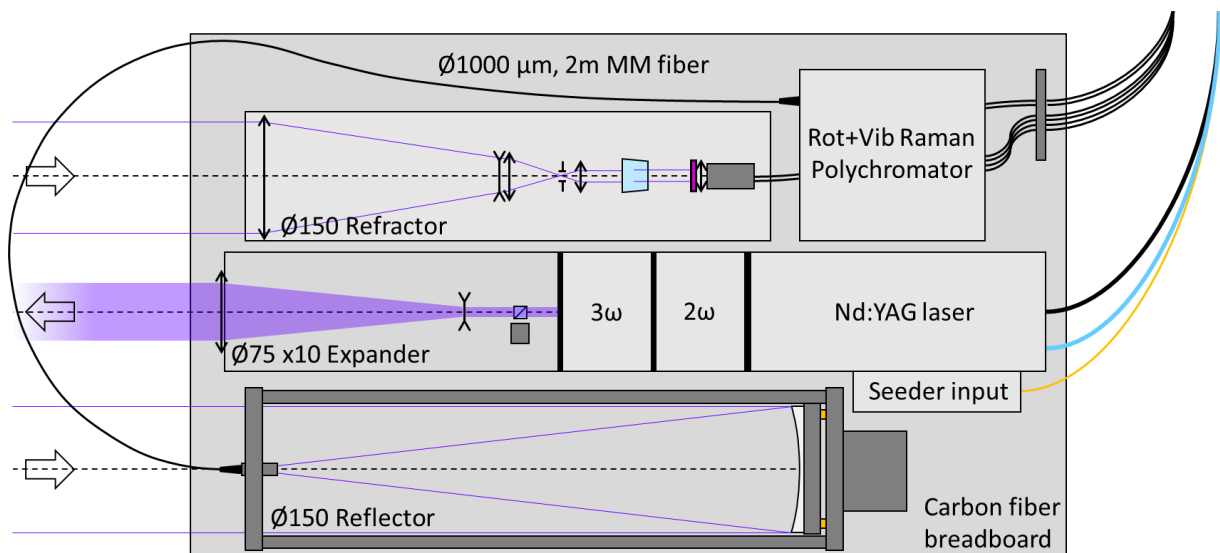
- 272 • As explained above, the atmosphere is assumed to be homogeneous in WVMR and
 273 temperature (down to $<0.5^\circ\text{C}$) up until z_∞ , whereas the overlap ratios must be constant
 274 (down to $<0.4\%$) after z_∞ . Also, the maximum range (with sufficient SNR) of the lidar
 275 must exceed z_∞ , implying nighttime measurements for the Raman channels. Therefore,
 276 the effects generating overlap variation after a few hundred meters must be prevented.
- 277 • The lidar is assumed to retain the exact same overlap functions when aiming
 278 horizontally and vertically. Considering a field of view around 1 mrad, the stability of
 279 the emission and reception optical paths must be better than ~ 10 μrad between these

280 two positions. This is feasible for a small refractor but difficult for a Raman system such
281 as WALI, with a heavy laser and large reflector.

282 These difficulties make it extremely challenging to estimate the overlap ratios with an accuracy
283 better than a few percent. This is enough for the WVMR, but we find that a correction must be
284 applied by comparing with in-situ sounding for temperature measurements by Raman lidar.

285 3 Implementation and bias mitigation on the WALI system

286 In this section, we describe the WALI instrument from the emitter to the reception channels,
287 characterizing the critical elements in the framework of WVMR and temperature
288 measurements. The system has evolved from its previous implementation described in Totems
289 et al. (2019), by adding RR channels and a fibered telescope receiver. A global diagram
290 presenting the main lidar sub-systems is shown in Figure 2, and a summary of its characteristics
291 is given in Table 2.



292
293 Figure 2. Global diagram of the lidar system. The main sub-systems are: the emitter (center),
294 the elastic receiver using a refractor (top), the Raman receiver using a fibered parabolic reflector
295 (bottom), and a separate, thermally stabilized polychromator (upper right). See Figure 5 for the
296 detail of the polychromator design.

297 Its main features are a single rotatable platform (lightweight carbon fiber breadboard by
298 CarbonVision GmbH) carrying both its emission and reception paths, a 150-mm refractor for
299 the elastic channels (for aerosol studies), and a 150-mm diameter parabolic fibered reflector for
300 all the Raman channels. The separation of the four Raman channels takes place in a deported
301 polychromator set in a thermally controlled enclosure, fed by the optical fiber. Fiber optics are

302 also known to partly scramble the input illumination, which could help minimize the range-
 303 dependance of filter transmittance or detector sensitivity for the different Raman channels. The
 304 output signals from the photomultiplier tubes (PMTs) in the polychromator are digitized by a
 305 NITM PXI system (not shown).

306 Table 2. WALI instrument characteristics summary (PRF: pulse repetition frequency, FOV:
 307 field of view, CWL: central wavelength in vacuum, FWHM: full width at half-maximum, OOB:
 308 out-of-band blocking specification, OD: optical density)

Emitter	Laser	Lumibird TM Q-Smart 450 SLM, tripled Nd:YAG, frequency stabilized $\lambda_{\text{laser}} = 354.725$ nm in vacuum, $E_p = 100$ mJ, PRF = 20 Hz.
	Optics	High-power polarizing beamsplitter and 10x beam expander Output beam diameter: 65 mm, Em/Rec separation: 200 mm
Elastic	Optics	Ø150 mm F/2 UV fused-silica refractor
receiver	Spatial filter	0.67 x 2 mrad FOV
	Spectral filter	CWL = 354.71 nm, FWHM = 0.22 nm, OOB: OD >4.0
Raman	Optics	Ø150 mm F/4 Newton reflector
	Spatial filter	Ø1.67 mrad FOV
receiver	Fiber optics	Ø1 mm, 2-m long, OH-rich multimode fiber
	VR spectral filters	365 nm longpass (OD >2) + 395 nm (OD >2) beamsplitter + Materion TM interference filters: N ₂ : CWL = 386.76 nm, FWHM = 0.27 nm, OOB: OD >4.0 H ₂ O: CWL = 407.59 nm, FWHM = 0.34 nm, OOB: OD >4.0
	RR spectral filters	365 nm shortpass (OD >2) + CWL = 355 nm, FWHM = 10 nm, flat-top, OOB: OD >6.0 + 50:50 non-polarizing beamsplitter + Materion TM interference filters: RR1: CWL = 354.09 nm, FWHM = 0.24 nm, OD >6.0 at 354.7 nm RR2: CWL = 353.22 nm, FWHM = 0.54 nm
Detection	Photodetectors	Hamamatsu H10721-210 photomultiplier tubes (PMT) with >0.13 A/W cathode sensitivity
	Amplification	Up to 2 10 ⁶ . Elastic & RR: fixed, VR: sky-background piloted
	Acquisition	3x NI TM PXI-5124 two-channel digitizers Sampling frequency: 200 MHz, 12-bit, Q-switch-triggered

Recording	1000 shots ($\Delta t_0 = 1$ min), 200 MHz ($\Delta z_0 = 0.75$ m)
	Analog + photon-counting

309 **3.1 Emitter**

310 The emitter is a commercial Lumibird/Quantel “Q-Smart 450” Nd:YAG pulsed laser, stabilized
 311 by injecting the output of a single longitudinal mode fiber laser emitting at 1064.175 nm into
 312 the main cavity (“SLM” option), and frequency-tripled to emit at wavelength
 313 $\lambda_{\text{laser}} = 354.725$ nm (in vacuum). The nominal pulse energy for the Q-Smart 450 with SLM is
 314 100 mJ at 355 nm, with a Pulse Repetition Frequency (PRF) of 20 Hz. These values set WALI
 315 near the eye safety limit for pulsed energy, making the system eyesafe at the output of a 2-meter
 316 funnel, as limited by leaks at 532 nm through the built-in filtering dichroic plates.

317 A critical issue to be cleared before using the Q-Smart 450 SLM in WALI was the spectral
 318 purity and stability of the laser, in terms of linewidth and wavelength drift. The laser seeder at
 319 1064.175 nm is specified with a 50 MHz (0.062 pm at 355nm) stability at fixed temperature,
 320 and 37 MHz $^{\circ}\text{C}^{-1}$ (0.046 pm $^{\circ}\text{C}^{-1}$ at 355 nm) temperature drift.

321 Nevertheless, the stability of the Q-Smart emission at 354.725 nm has been verified with a
 322 dedicated optical setup, sending the output of a Michelson interferometer with optical path
 323 differences (OPD) between 0 and 100 mm on a UV-sensitive CCD camera. By extracting the
 324 contrast and phase variations of the fringes at large OPDs from the videos, we were able to
 325 ascertain:

- 326 • the laser linewidth, without seeder, to be 24 ± 2 pm (versus 26.5 pm datasheet value), and
 327 with seeder, to be small compared to 1 pm (versus 0.2 pm datasheet value),
- 328 • the wavelength drift, without seeder, to be below 8 pm over 10 minutes, and with seeder,
 329 to be below 0.2 pm RMS (root mean square fluctuations) over 5 minutes. We consider
 330 the remaining fluctuations to be mostly due to the ~ 0.05 pm $^{\circ}\text{C}^{-1}$ temperature-linked
 331 drift of the seeder, which is not temperature-controlled and was recently turned on.

332 Given the requirements derived in Section 2.3, this makes the seeded Q-Smart laser
 333 theoretically suitable for RR measurements of temperature.

334 **3.2 Raman receiver**

335 In this sub-section we discuss the possible impact on the VR/RR ratios of the fibered reflector
 336 (beam scrambling and fiber optics fluorescence), of Raman filters characteristics, and of the

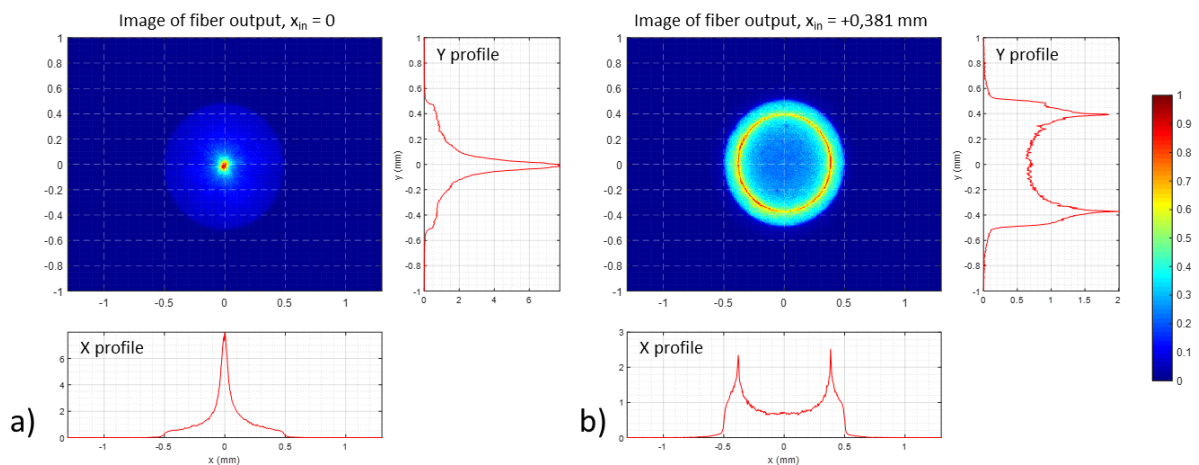
337 polychromator design and alignment. As far as we know, this type of comprehensive study does
338 not exist in the literature for Raman lidars.

339 3.2.1 Fibered reflector telescope and scrambling of the lidar field-of-view

340 The elastic and Raman receivers are both 150 mm in diameter. The focal length of the refractor
341 (elastic channels) is ~ 300 mm, which with a $200 \times 600 \mu\text{m}$ field stop achieves full overlap at
342 $\sim 150\text{-}200\text{m}$. However, the focal length of the reflector (Raman channels) is 600 mm (parabolic
343 mirror with aperture F/4); this implies using a multimode fiber optics about 1 mm in diameter
344 as the field stop to allow similar results in terms of field-of-view and overlap. The chosen fiber
345 optics is an OH-rich UV fused silica fiber, 2 m in length and $1000 \mu\text{m}$ in core diameter, with
346 numerical aperture 0.22 (Avantes FC-UV1000-2).

347 Coupling the reflector output into a multimode fiber (e.g. Chourdakis et al., 2002) allows: i) to
348 minimize occultation of the primary mirror (here only 12 mm in diameter), ii) to deport the
349 Raman channel separation away from the telescope, making it a separately tunable optical
350 system, minimizing the overall lidar size and making light or temperature confinement easier,
351 iii) in theory, to scramble the fiber output illumination versus the lidar field angle, therefore
352 minimizing the range-dependence of AOIs on the IFs discussed in Section 2.3, and flattening
353 overlap ratios after the geometrical full-overlap distance.

354 The scrambling of the lidar field-of-view, via the multiple internal reflections in the fiber, has
355 been experimentally tested by imaging the output of the fiber, with a varying point-like input.
356 The results are shown in Figure 3. Note that the radial coordinate of the output point relative to
357 the center of the fiber corresponds to a given AOI on a well-aligned IF in the following
358 polychromator, after a $f^\circ = 50$ mm doublet lens.



359

360 Figure 3. Images of the output facet of the 1 mm diameter multimode fiber optics for a) centered
361 and b) decentered (at $x_{in} = 0.38$ mm horizontal offset from the center of the core) input point of
362 a 20-mm beam focused on the input facet of the fiber, and energy density profiles along the x
363 and y axes.

364 It appears on Figure 3 b) that the input energy is mostly redistributed tangentially (i.e. along the
365 angular polar coordinate, as opposed to radially) by its passage through the fiber. The radial
366 dispersion remains small, and the mean output radius is approximately equal to the input radial
367 coordinate. Manually applying curvature to the fiber, as suggested by so-called “mode
368 scrambling” devices, did not make the energy distribution more uniform so much as creating
369 unwanted losses (effect not shown). Even for a centered input, the energy radial distribution –
370 i.e. the percentage of the total output in a given radial bin, that will therefore impact a well-
371 aligned filter at the same AOI – is uniform. We conclude that even with the use of fiber optics
372 the angle of incidence on the interference filters depends on the image positions in the focal
373 plane of the telescope (i.e. mainly the distance to the optical axis), in contrast to what could be
374 expected. Range-dependent biases will not be strongly mitigated.

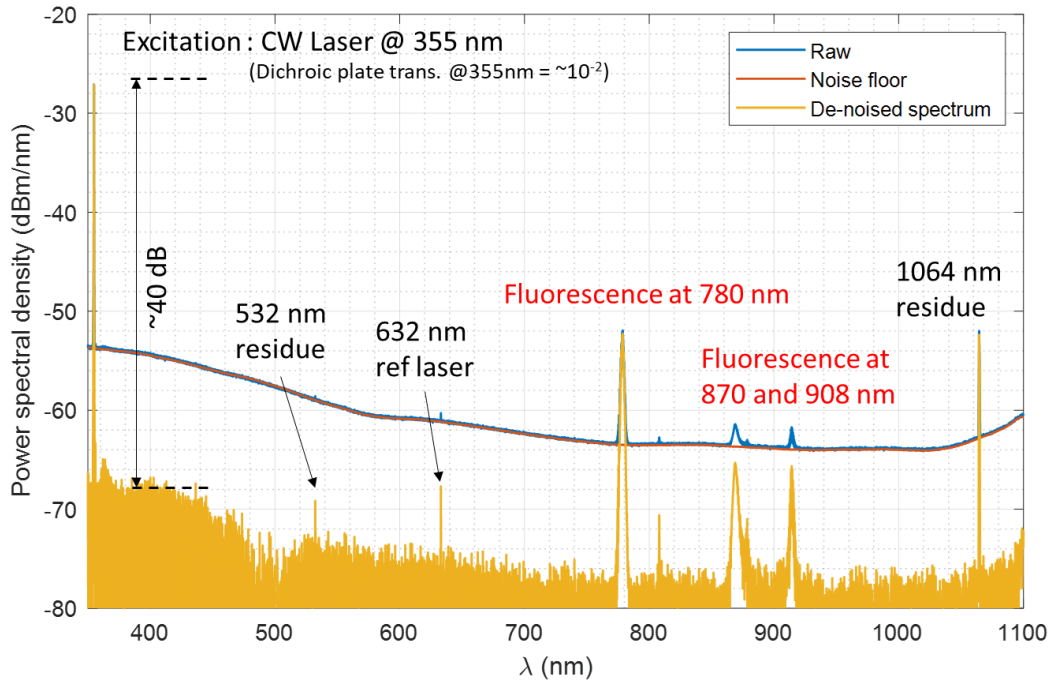
375 3.2.2 Fiber optics fluorescence

376 It has been shown by Sherlock et al. (1999) and discussed by Whiteman et al. (2012) that fiber
377 optics fluorescence could be an obstacle to water vapor measurements, because elastic
378 scattering at 532 nm was inducing fluorescence in an OH-poor fiber at a non-negligible level
379 compared to the atmospheric Raman scattering. It was solved by using an OH-rich fiber, but it
380 was predicted in the latter work that the effect could be larger at 355 nm.

381 We have characterized this effect in the WALI fiber optics, using a narrowband CW laser
382 excitation centered at 355 nm. The output of the fiber was analyzed by a Fourier transform
383 spectrometer (Thorlabs OSA201C spectrum analyzer), behind a longpass dichroic plate cutting
384 the direct laser emission, and the same collimating achromat as in the polychromator. The
385 resulting spectrum is shown in Figure 4.

386 We plot both the raw spectrum and the Fourier transform spectrometer noise floor after 1000
387 profile integrations, to highlight the very weak features observed at 780 to 910 nm, and the high
388 associated uncertainty. Due to the noise level, and given the dichroic plate residual
389 transmittance of the laser wavelength, we can only ascertain that the fluorescence power
390 spectral density (PSD) around 400 nm is lower than 10^{-6} times the peak laser PSD, although no
391 feature can be detected in this spectral domain. Note that fluorescence between 400 and 500 nm
392 was indeed observed using a broadband excitation from a fibered LED at 340 nm (not shown).

393 Nevertheless, the amount of rejection observed for a 355 nm excitation is sufficient to exclude
 394 an adverse impact of the OH-rich fiber optics for Raman lidar measurements.
 395



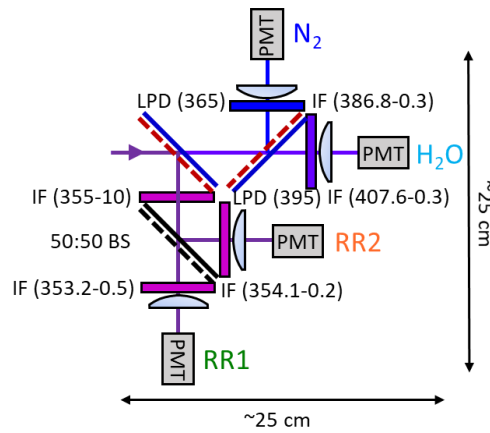
396
 397 Figure 4. 1000- μ m diameter, 2-meter long fiber fluorescence measurement with 355 nm laser
 398 illumination.

399 3.3 Raman channels

400 3.3.1 Polychromator configuration

401 The RR+VR polychromator configuration used in WALI is presented in Figure 5. Dichroic and
 402 non-polarizing beamsplitters are used to separate the channels. In contrast to the design of
 403 Hammann et al. (2015) which optimizes throughput and laser-line rejection on the RR channels,
 404 we chose to implement a splitter-based configuration, favouring a compact system (25x25 cm,
 405 easier to confine) and normal incidence on the filter, at the expense of SNR. Indeed, designing
 406 the filters for a correct CWL at 5° incidence (as in the cited work) instead of 0° dramatically
 407 narrows the filter angular acceptance, as can be deduced by deriving Eq. (15) as a function of
 408 incidence θ' . In the WALI polychromator, the output from the fiber is collimated by a near-UV
 409 achromat with 50 mm focal length, resulting in a 22 mm diameter beam. Dichroic beamsplitters
 410 with adequate cut-on wavelengths are used to separate channels. On each separated channel, an
 411 aspheric lens condenses light on the PMT surface, located 4 mm before the focal plane. A steel

412 cage system assembly holds all parts with great stability, however beamsplitters are not always
 413 perfectly aligned at 45° in the stock cage cubes. That is why all filter, lens and PMT sub-
 414 assemblies are mounted on tiltable mounts to allow precise alignment at normal incidence.

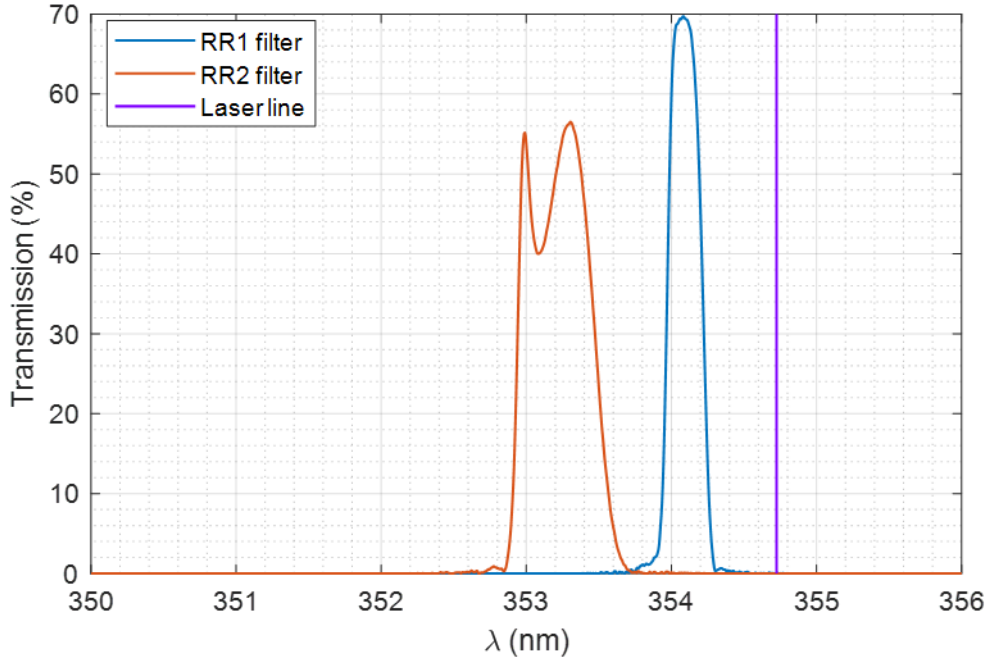


415
 416 Figure 5. Compact rotational & vibrational Raman separation configuration used in WALI. IF:
 417 interference filter (with CWL - FWHM given in nm), BS: beam splitter, LPD: long-pass
 418 dichroic beamsplitter (with cut-off wavelength given in nm), PMT: photo-multiplier tube. This
 419 polychromator is thermally regulated in a dedicated light-tight enclosure.

420 3.3.2 Filters qualification

421 All interference filters were custom-made by Materion, including the RR filters on
 422 specifications graciously shared by the team of A. Behrendt (following Hamann et al., 2015).
 423 They were characterized on the Fourier transform spectrometer (described in section 3.2.2)
 424 prior to mounting, using fibered LEDs peaking at 340, 385 and 405 nm as the light source; the
 425 beam was collimated by the same near-UV achromat with 50 mm focal length. We give the
 426 measurements results for the RR filters in Figure 6 and Table 3.

427 The effective index and angular acceptance of the filters (arbitrarily chosen for a 10% loss at
 428 the CWL) were assessed by tilting the filters of a known angle. A critical parameter, the
 429 transmittance of both filters at the laser line λ_{laser} in operational conditions was assessed on the
 430 lidar itself, by measuring the energy of an echo on a hard target located at 200 m, and switching
 431 between an elastic IF of known transmittance with a known strong optical density and the RR
 432 IF in question. The excellent extinction in the RR1 filter guarantees a minimal effect of elastic
 433 signal leak in temperature retrievals, but it was nevertheless subtracted as in Eq. (3). Note that
 434 no significant echo was detected on the H₂O-Raman channel, indicating extinction better than
 435 a few 10⁻⁹, thanks to the two dichroic plates.



436

437 Figure 6. RR filters spectral transmittance measured on optical spectrum analyzer with
 438 illumination by a 340 nm LED: RR1 (low-J) and RR2 (high-J) filter at 0° incidence.

439 Table 3. Measured RR IF characteristics. All CWL values are given in vacuum.

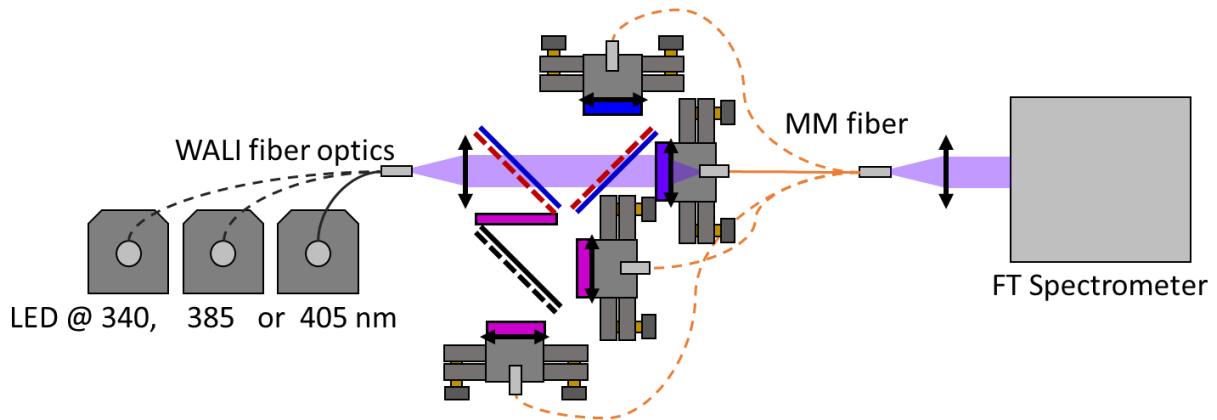
	RR1 filter	RR2 filter	Uncertainty
CWL	354.09 nm	353.22 nm	0.01 nm
FWHM	0.24 nm	0.54 nm	0.01 nm
n_{eff}	1.62	2.03	0.05
Max transmittance	69%	51%	5%
Laser line transmittance	$2.7 \cdot 10^{-8}$	$2.9 \cdot 10^{-7}$	10% relative
Angular acceptance (AOI for 10% loss at CWL)	1.5°	2.5°	0.2°
CWL shift at max field angle (i.e. edge of fiber, AOI = 0.59°)	-9.8 pm	-2.5 pm	0.3 pm

440 3.3.3 Polychromator alignment and qualification

441 Due to the filter CWL shift evolving as the square of the AOI in Eq. (15), it is essential to
 442 minimize range-dependent biases by aligning the filters at a precisely normal incidence from
 443 the input beam. However off-the-shelf beam splitter plate holders are found to be misaligned

444 by up to 1° from an ideal 45° incidence. All PMTs are mounted jointly with their own IF and
445 lens into a tiltable mount to correct for this (represented on Figure 7).

446 The alignment of these mounts is performed in the lab by conjugating an input multimode fiber
447 of $600\ \mu\text{m}$ diameter replacing the lidar input, into a target fiber $200\ \mu\text{m}$ in diameter at the focus
448 of the PMT lens, through the polychromator. Fibered LEDs are used for illumination like in
449 section 3.3.2. All the channels are sequentially addressed in this manner. By obtaining a
450 maximal energy and a radially uniform profile at the output of the target fiber, one can ensure
451 alignment with a precision of 0.1 to 0.3° .



452
453 Figure 7. Method for polychromator alignment validation. Light from LEDs is input in the
454 WALI fiber optics, passes through the polychromator, and into a multi-mode fiber (MM fiber,
455 $\text{\O}600\ \mu\text{m}$) analysed by a Thorlabs OSA201C Fourier transform spectrometer. Channel central
456 wavelengths are expected not deviate from those of the filter measured independently at normal
457 incidence, to validate alignment.

458 To verify the result, the spectral transmittance of the polychromator channels themselves are
459 characterized by the Fourier transform spectrometer, as shown on Figure 7. By illuminating the
460 channel with a LED coupled in the actual lidar fiber, we ensure that the polychromator is studied
461 in operational conditions. The CWL of each channel is expected not deviate by more than 20
462 pm (twice the empirical accuracy) from the CWL measured on the individual filter at normal
463 incidence, to validate the alignment. The polychromator aligned using the procedure proposed
464 above passes this test.

465 3.4 Detectors

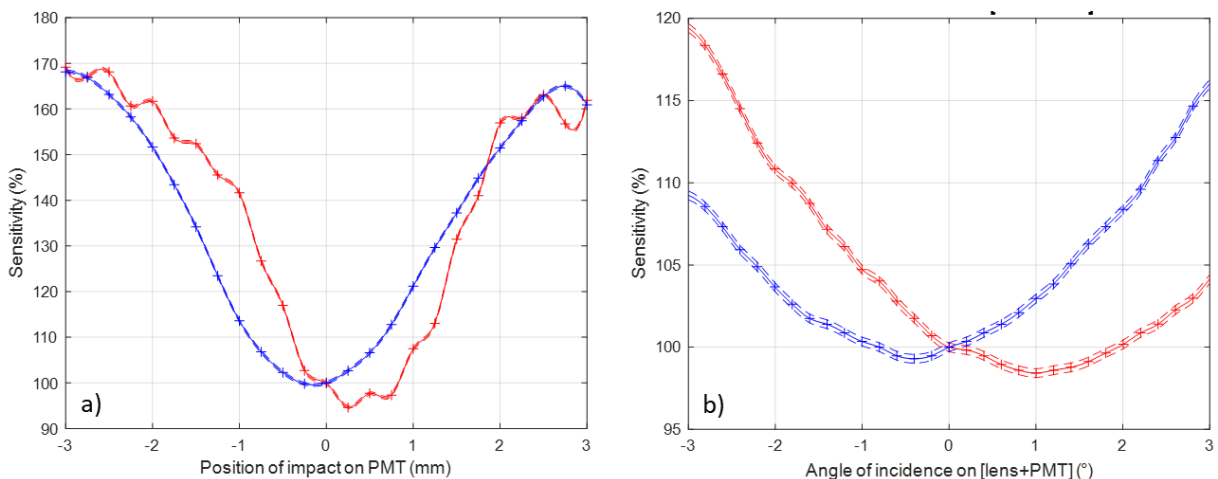
466 Hamamatsu 10721P-210 PMTs, with $>0.13\ \text{A W}^{-1}$ cathode sensitivity at 400 nm, and up to
467 $\sim 2 \cdot 10^6$ controllable internal gain, are used to transform the optical flux into an electric current,
468 directly digitized at 200 MHz ($0.75\ \text{m}$ sampling along the line of sight) by three NI PXI-5124

469 two-channel digitizers with $50\ \Omega$ load. The acquisition software, custom-made with Labview,
 470 conducts analog and photon-counting (thresholding at ~ 3 standard deviations of the noise)
 471 accumulations in parallel during 1000 shots (50 seconds), every minute, which are then pre-
 472 processed and recorded (~ 10 seconds down time). Every ~ 8 minutes, baselines are recorded
 473 with PMT gains set at zero. The next sub-sections describe critical points of the detectors
 474 affecting the RR and VR channel ratios.

475 3.4.1 PMT response variability

476 As explained in Section 2.3, the non-uniformity of the PMT response can affect the ratios of
 477 Raman channels as a function of range. We tested the sensitivity profiles of WALI's H_2O -
 478 Raman PMT to continuous laser illumination at 405 nm wavelength, first using a 1-mm
 479 diameter collimated beam, as a function of both point and angle of incidence. A cumulated ~ 6.0
 480 neutral density filter was used to avoid saturation of the PMT.

481 As shown on Figure 8 a), a strong variation of sensitivity by a factor of almost 2 is found on the
 482 PMT surface, much larger than specified. The relative sensitivity is lowest near the center of
 483 the PMT and highest on the sides, on a diameter of 4 mm approximately equal to the spot size
 484 in the lidar. Indeed the PMT surface is 4 mm before the focal plane of the 0.5 NA condensing
 485 aspheric lens. This is consistent with the results of Simeonov et al. (1999) on an older generation
 486 of detectors, excluding a suspected hole-burning phenomenon over the lifetime of our PMT.
 487 On the vertical axis, we also note the effect of the gridded cathode. Note that sensitivity does
 488 not vary by more than a few percent as a function of angle of incidence (not shown).



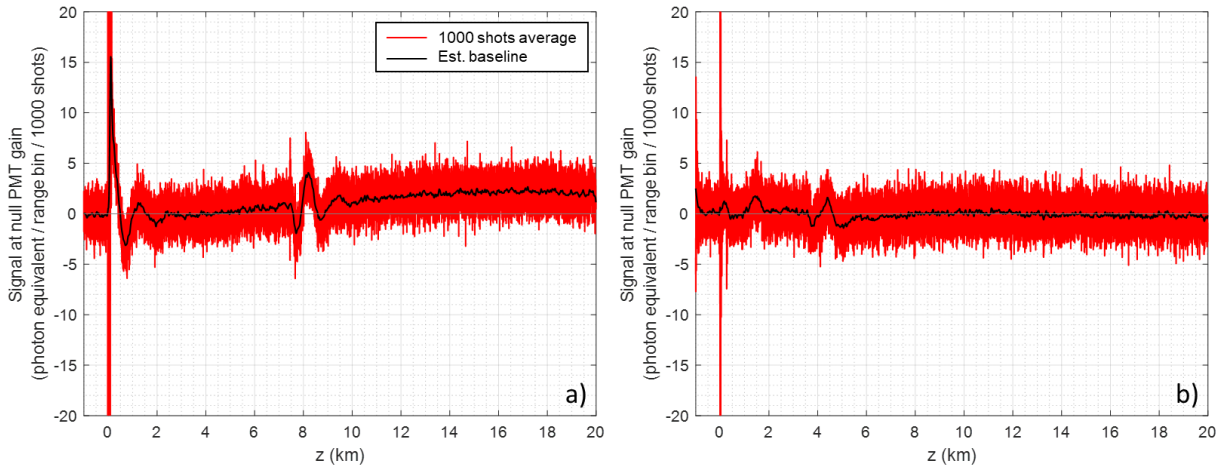
489
 490 Figure 8. Study of the non-uniformity of the PMT response: a) as a function of point of impact
 491 on the active area along the horizontal (blue) and vertical (red), with a 1 mm collimated beam
 492 from a 405 nm laser, b) as a function of angle of incidence on the lens and PMT assembly
 493 similar to the ones used in the WALI polychromator, with a 22 mm collimated beam from the

494 same laser. Dashed lines represent uncertainty calculated over multiple measurements.
495 Sensitivity is given normalized by its value at the approximate mechanical centre of the PMT
496 or at normal incidence as determined using the reflection on the attached neutral density filter.
497 We then put the condensing lens used in the polychromator in front of the PMT, and studied its
498 response as a function of AOI on the lens+PMT assembly, which is shown in Figure 8 b). The
499 input beam was the nominal size in the polychromator ie. ~22 mm in diameter. We find that the
500 curve corresponds well to the measured sensitivity profile, smoothed by its convolution with
501 the spot on the PMT. The problem is that at normal incidence, the derivative of sensitivity with
502 incidence is 2-5% per degree. Using the calculations in Section 2, a $\theta = 1$ mrad field angle
503 corresponds to 0.39° incidence on the PMT, inducing potentially 0.8-2% bias on R and Q , and
504 thus a significant 1 to 2°C bias on temperature. In the future, the condensing lenses will be
505 replaced with afocal beam reducers to reduce this dependency.

506 3.4.2 Baseline and EM parasites correction

507 The baseline induced by the detection chain is found to vary between channels and in time. It
508 is also subject to electro-magnetic (EM) interference causing parasitic signals of both high
509 frequency, mostly due to the flashlamp high peak current radiating over the system, and low
510 frequency, probably due to other neighboring electronics. For this reason, the channel baselines
511 are evaluated regularly (by averaging 1000 shots with PMT gain set to zero, every 8 minutes),
512 smoothed and corrected (L_j in Eq. (2)). However, for the Raman channels (H_2O and RR2
513 specifically), the weakness of the signals requires a specific care of EM compatibility, as
514 repeating parasitic spikes were found to jam the channels (especially photon counting which
515 relies on thresholding) starting at altitude 6-7 km.

516 Figure 9 a) shows an example of perturbed baseline. Trial and error established that common
517 methods to avoid ground loops were not all efficient: star grounding of the various cables
518 worsened the problem, whereas physically separating coaxial signal cables from direct current
519 power supply and control voltage cables, and grounding all connectors and opto-mechanics
520 again on the breadboard side, mitigated it, reaching the baseline plotted in Figure 9 b). Note
521 that baseline variation is not significant between successive evaluations without an external
522 perturbation; the estimated baseline is automatically subtracted from the profiles before
523 recording during the next 8 minutes (Eq. (3)).



524

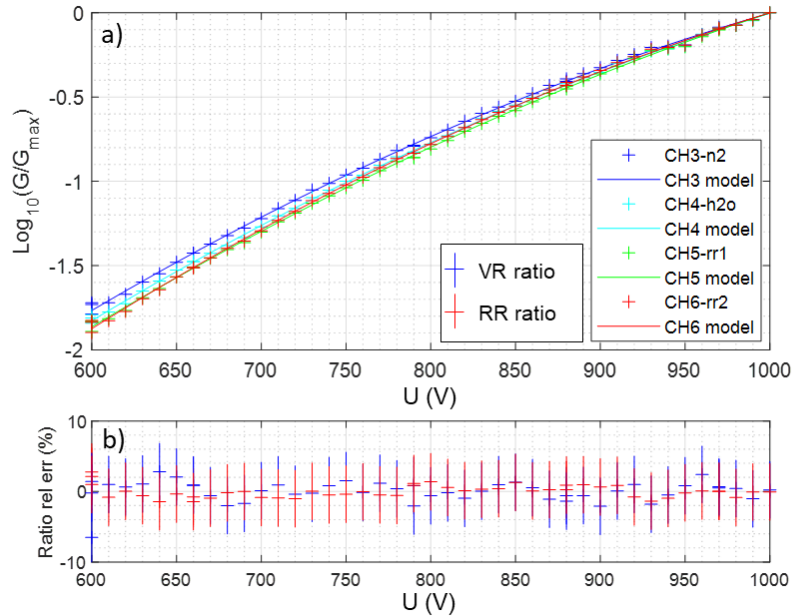
525 Figure 9. Analog detection baseline measurements (red) over 1000 laser shots with PMT gains
 526 set to zero, expressed in photon counts equivalent on the RR2 channel: a) in an unfavorable
 527 case (no mitigation), showing both baseline fluctuations over time (20 km \sim 133 μ s) and strong
 528 electro-magnetic parasites at large distance; b) on the WALI system, after mitigation. The final
 529 estimated baseline ($\hat{L}_j(z)$ in Eq. (3)) obtained after smoothing, which is subtracted to all
 530 recorded profiles, is in black.

531 3.4.3 PMT gain adaptation

532 On each channel, PMT internal amplification gain G (using photoelectron multiplication) is a
 533 definite function of its control voltage U . The variation of G by ~ 2 orders of magnitude allows
 534 for the optimization of the dynamic range. This helps deal with the different Raman cross-
 535 sections in each filter, with variations of atmospheric transmittance, and especially with sky
 536 background levels during daytime. The gain is pushed at its maximum possible value still
 537 satisfying two conditions: i) the signal voltage maximum does not exceed the range of the
 538 digitizer, ii) the sky background signal does not exceed the maximum output current of the PMT
 539 that guarantees linearity (100 μ A, ie. $\langle S_{raw} \rangle < 5$ mV). This is indispensable for day-round
 540 measurements of WVMR, otherwise the channels would be saturated during daytime (Chazette
 541 et al., 2014b), or suboptimal in SNR during nighttime.

542 However, PMT gain adaptation leads to biases on the Raman channel ratios if the gain versus
 543 control voltage characteristics are not known with a better precision than the requirements
 544 stated in Table 1 (2% on VR channels, 0.4% on RR channels). In Figure 10 a), we show the
 545 experimental calibration of G versus U as well as second-degree polynomial fits for each
 546 channel. The relative error on the VR and RR channel gain ratios approximated by these models
 547 is plotted on Figure 10 b), with the measurement uncertainty. This uncertainty is mostly due to

548 variations of atmospheric parameters and laser energy during calibration. Since all relative
 549 errors are well centered, we compute that the possible error for the gain ratio with these models
 550 is $\sim 1.3\%$. This is compatible with WVMR measurements but not with temperature
 551 measurements. Therefore, the PMT gain should only be adapted on the VR channels, and the
 552 RR channels should be kept at a fix value of gain.



553
 554 Figure 10. Calibration of PMT gain G versus control voltage U : a) log-gain measurements and
 555 second-degree polynomial model for all Raman channels, and b) relative gain ratio error
 556 between model and measurements for vibrational and rotational Raman channel ratios.

557 3.4.4 Merging analog and photon-counting signals

558 Both analog and photon-counting raw signals are recorded. The analog signal has lesser SNR
 559 at high altitude during nighttime, whereas the photon-counting signal is saturated at low altitude
 560 and by daylight; by merging them correctly, an optimal SNR can be obtained (Newsom et al.,
 561 2009). For signal processing, the photon-counting raw signals are first desaturated (details in
 562 Chazette et al., 2014b). Merging is performed during nighttime on the pre-processed signals
 563 defined in Eq. (3). After calculating a photon to Volts conversion constant at an altitude where
 564 photon-counting is not saturated, the converted photon-counting profile replaces the analog
 565 profile after a predefined altitude depending on signal strength (from 1 km for the H₂O VR
 566 channel, up to 4 km for the elastic channel).

567 We wish to emphasize here that baselines L_j and background signals B_j in Eq. (3) must be
 568 estimated separately for the analog and photon-counting recorded profiles (which have no

569 baseline, and a smaller but non-zero background value due to the suppression of electronic
570 noise). Otherwise, the merged signal will show discontinuities at the cut-off altitude, and biases
571 at high altitude at dusk and dawn. Their impacts are typically much larger than the requirements
572 of Section 2.2.

573 **4 Qualification on the atmosphere**

574 In this section, we qualify the WALI system starting with the measurement of its overlap factor
575 ratios, followed by its calibration and comparisons with radiosoundings. Remaining biases are
576 highlighted and corrected, and experimental measurement errors are evaluated.

577 **4.1 Experimental set-up and strategy**

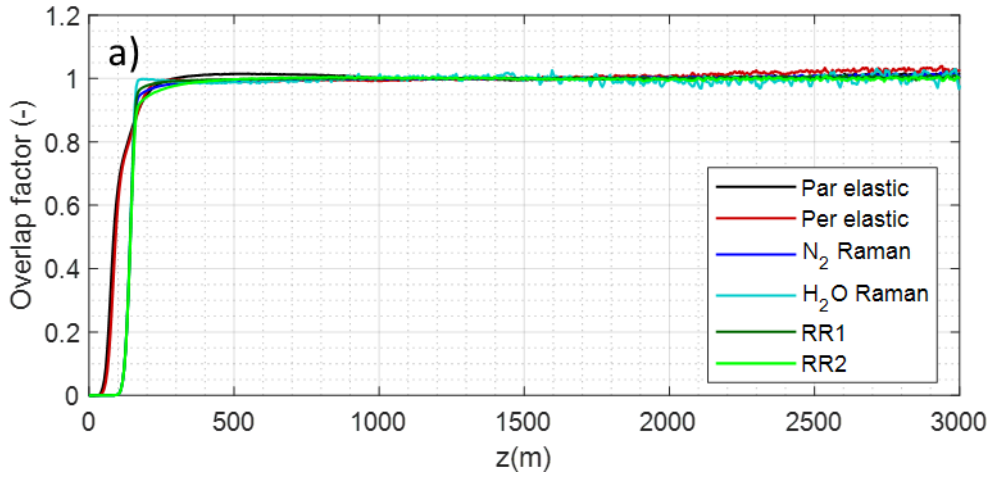
578 We put the lidar into operation in our laboratory near Saclay (48°42'42"N 2°08'54"E) over a
579 period of two weeks in May 2020. It was placed on a rotating platform below a trapdoor
580 equipped with silica windows for zenith shots, and in front of a window at a height of about 9
581 m above the ground level (agl) for horizontal shots. During the latter, the lidar aimed North <5°
582 above the horizon (beam elevation <80 m per km of range). In that direction, land use is fields
583 up to 800 m range, buildings and trees between 800 and 2 km range, and fields again up to 5.5
584 km range.

585 To calibrate and qualify the lidar measurements, we use radiosoundings launched two to three
586 times daily from the operational Météo-France station located in Trappes (48°46'27"N
587 2°00'35"E), 12.3 km WNW from the lidar near Saclay, approximately upstream in the
588 prevailing winds, although the wind was oriented mostly NE during the May 2020 period.

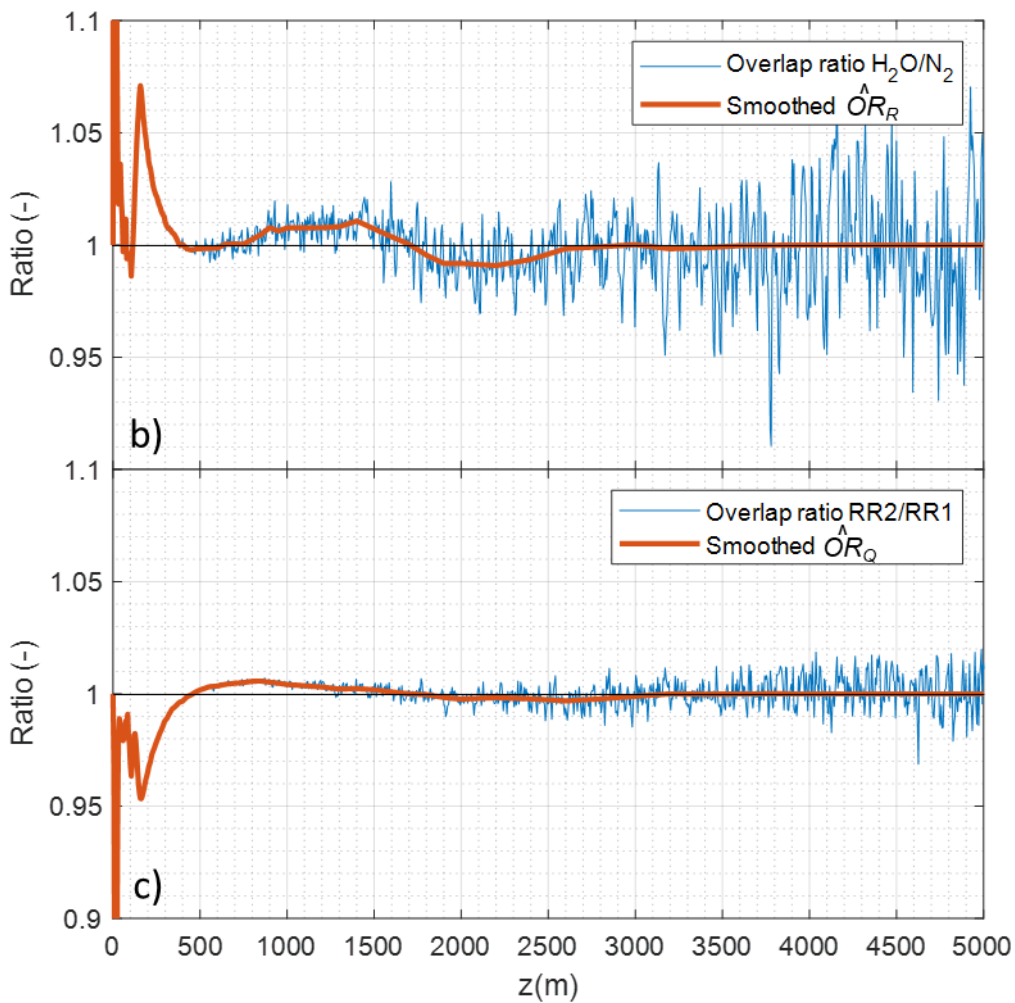
589 **4.2 Measurement of overlap ratios with horizontal shots**

590 The overlap factors and their ratios were estimated on signals averaged over 3 hours after sunset
591 on December 19th, 2019, with a tepid (14°C), non-turbulent but hazy atmosphere (aerosol
592 extinction coefficient 0.32 km^{-1} at 355 nm with Angström exponent ~ 1.5 , 11°C ground
593 temperature, and WVMR at ground level around 6.5 g kg^{-1}). With a planetary boundary layer
594 (PBL) height of ~ 900 to 1000 m, and slow gradients of temperature (-1 to -4°C km^{-1}) and
595 WVMR (-0.8 to $-1.2 \text{ g kg}^{-1} \text{ km}^{-1}$) in that PBL (as measured by radiosoundings launched from
596 Trappes at $\sim 12:00\text{UTC}$ and $0:00\text{UTC}$, presented in the next subsection), conditions were
597 excellent for a homogeneous atmosphere within the first 5 km at least.

598 The estimated overlap factors of the different channels, with atmospheric extinction fitted
599 between 800 and 2000 m, are shown in Figure 11 a). Full geometrical overlap is obtained as
600 expected between 150 and 200 m, but the curves differ by several percent between the Raman
601 channels. Atmospheric extinction drifts from the estimated value after 2 km.



602



603

604 Figure 11. a) Overlap factors measured over 3 hours of nighttime measurements with a
605 horizontal line-of-sight on Dec. 19, 2019. Estimated overlap ratios between VR (b) and RR (c)
606 channels: native resolution (thin blue line), final estimate after smoothing (thick red line).

607 The estimated ratios of overlap factors OR_R and OR_Q are plotted in Figure 11 b) and c), at 7.5 m
608 resolution (thin line) and after smoothing (thick line, final correction used hereafter). Peak
609 divergence is 5 to 7 %, at ~150 m. Convergence within 1% happens at ~400 m, but oscillations
610 of lower amplitude persist until ~3 km. We note that for OR_Q , deviations do not exceed the
611 $\pm 0.7\%$ required to maintain bias below 1°C. They are nevertheless corrected.

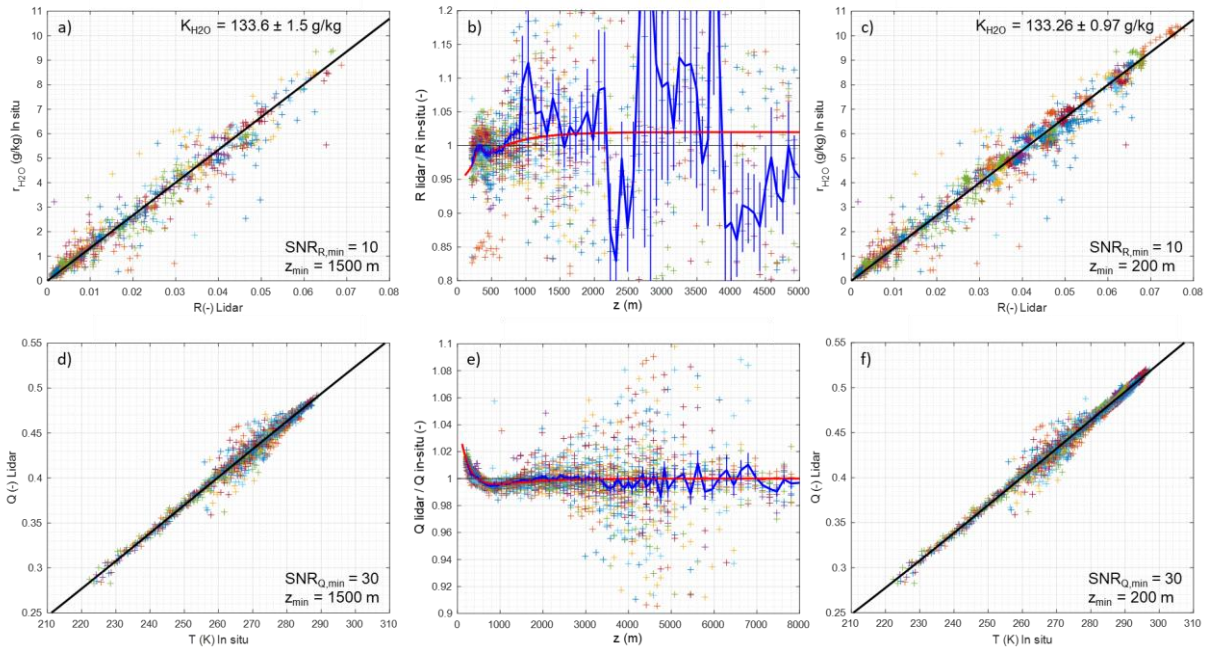
612 **4.3 Comparison to radiosoundings and calibration, estimation of residual error**

613 12 nighttime and 24 daytime radiosoundings were launched from Trappes between May 20th
614 and June 2nd, 2020. Lidar profiles are averaged from 0 to 40 minutes after the radiosounding
615 launch time. The range averaging is progressive and defined to keep the night time temperature
616 error below 1.5°C: range bins are 15 m long below 100 m agl, growing to 360 m above 8 km
617 agl.

618 In order to debias WVMR and temperature measurements from residual errors on OR_R and
619 OR_Q , we perform a three-step calibration:

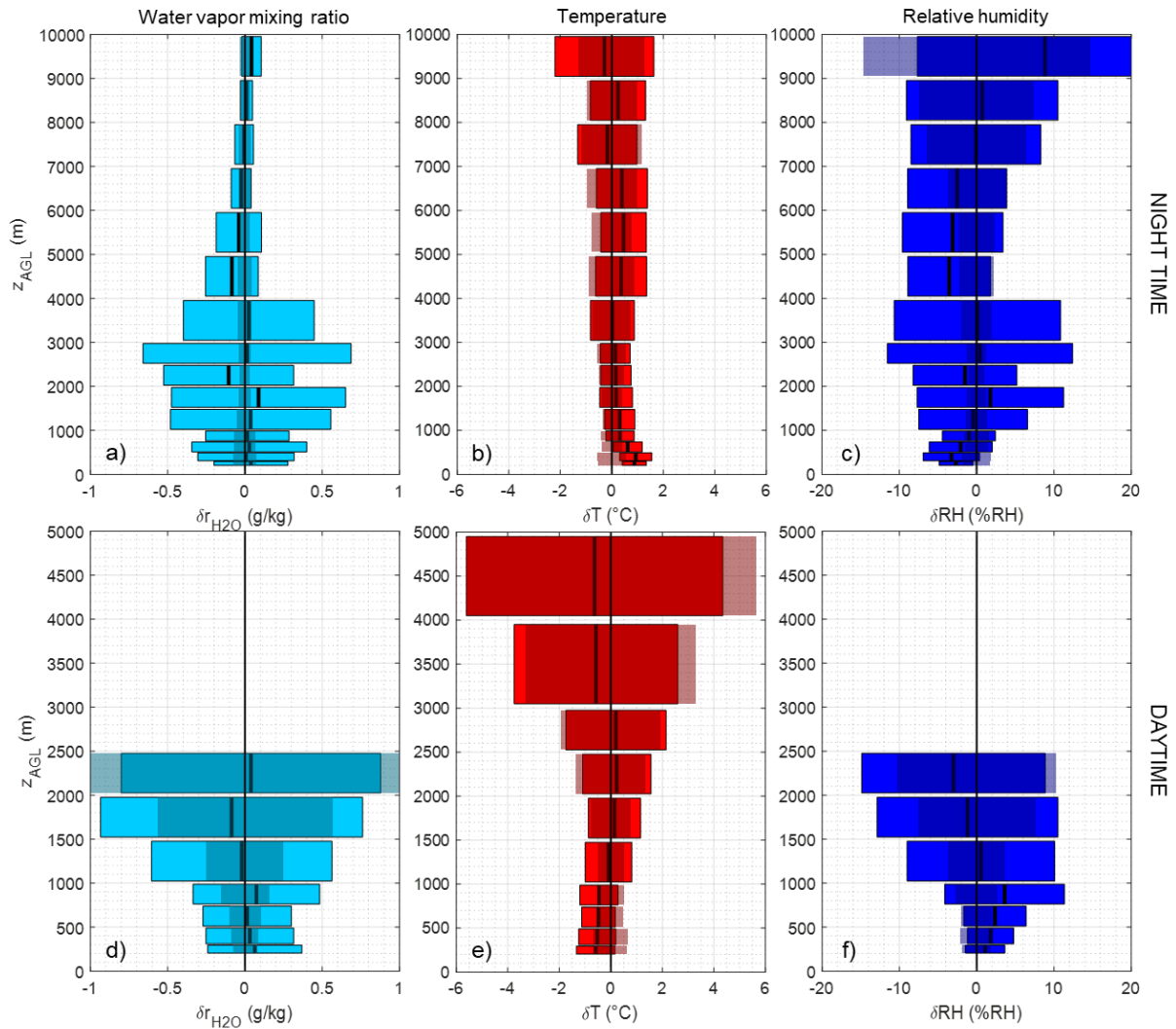
- 620 • First step: we exclude the first 1500 m agl of the profiles when fitting r_{H_2O} *in-situ* vs R'
621 and Q' vs T *in-situ* to estimate K and f respectively. This initial calibration is shown in
622 Figure 12 a) & d).
- 623 • Second step: using these first estimates, we then plot the ratios between the lidar
624 observables R' & Q' and the expected observables deduced from the in-situ
625 measurements and these initial calibration parameters. This provides an estimate of the
626 remaining biases on OR_R and OR_Q , which we find to be up to ~4% and ~1.8%
627 respectively. This represents a small correction to the overlap ratios estimated while
628 shooting horizontally, but remains larger than the requirements of precision specified in
629 Table 1. The modelled corrections of OR_R and OR_Q are plotted in red in Figure 12 b) &
630 e). We fit a sum of three exponential falls to the mean, of the form: $1 + a_1 \exp(-z/z_1) +$
631 $a_2 \exp(-z/z_2) + a_3 \exp(-z/z_3)$, with a_i coefficients and z_i ranges to be adjusted.
- 632 • Third step: we apply the previous estimates of OR_R and OR_Q and we perform a new
633 calibration using all the data (down to 200 m agl), yielding more precise estimates of
634 calibration constants, as shown in Figure 12 c) & f).

635 In the three steps, data with SNR lower than 10 for R' and 30 for Q' are rejected so as to
 636 limit the impact of noise present at higher altitudes.



637
 638 Figure 12. Results of calibration on 12 nighttime and 24 daytime radiosoundings launched from
 639 Trappes between May 20th and June 2nd, 2020 for WVMR (upper row) and temperature (lower
 640 row), in three steps: calibration on measurements above 1500 m (a/d) with samples as crosses
 641 (one color per radiosonde) and calibration curve in black; residual overlap ratio estimation (b/e)
 642 with samples as crosses, mean ratio in blue, random error on mean ratio as vertical bars, and
 643 model in red; calibration on all results (c/f). Daytime samples are limited to SNRs above 10 for
 644 R' (WVMR) and 30 for Q' (temperature).

645 The reliability of this calibration along time has been tested by comparing to the same exercise
 646 performed two months later at the end of July 2020. After calibration in the same conditions
 647 than in May, we found K decreased by $\sim 7.3\%$, and the temperature associated to a given value
 648 of Q' to be $\sim 2.1^\circ\text{C}$ higher. However, OR_R and OR_Q were still accurate within the reachable
 649 precision, ie. $\sim 0.2\%$. It was later proven that a malfunction of the laser seeder was responsible
 650 for a slow drift of the emitted wavelength. Thus, although a regular verification of the
 651 calibration is necessary, the measurement of the overlap ratios is reliable.



652

653 Figure 13. Residual deviations between lidar and Trappes radiosoundings in terms of WVMR,
 654 temperature and relative humidity, for night time (a/b/c) and daytime (d/e/f), with mean
 655 deviation (thick lines), and RMS error (colored rectangles). The error corresponding to noise
 656 levels on the lidar signal is shown as darker rectangles. Cloudy profiles have been discarded.
 657 Daytime measurements are limited to SNRs above 5 for R (WVMR) and 20 for Q (temperature).

658 In Figure 13, we examine the residual deviations between the lidar and the same series of
 659 radiosoundings used for the calibration. RH has been derived using Eq. (14) from lidar-
 660 estimated WVMR and temperature, and the pressure profile given by radiosoundings. For each
 661 parameter r_{H2O} , T and RH , we plot for daytime and night time profiles the mean and RMS
 662 deviations averaged over large range bins as colored bars, as well as the propagated signal error
 663 as darker shaded areas. This allows to compare the observed random error to what could be
 664 expected from the level of noise on the lidar measurements. Note that only profiles with good
 665 SNR unperturbed by clouds have been selected for this comparison.

666 On WVMR, the results show little bias, and RMS deviation is dominated by spatial atmospheric
667 variability at night and at low altitude (when SNR is high), and by lidar noise in all other cases.
668 On temperature, most of the RMS deviation is explained by noise; a significant +1°C bias is
669 seen below 800 m during nighttime, opposed by a -0.5°C bias during daytime. This could be
670 due to local effects in the diurnal cycle between LSCE and Trappes, although no such effect
671 can be significantly highlighted in weather model reanalyses (described below). On Figure 13
672 c) and f) are plotted the consequences of this bias on relative humidity RH to be around 2 to
673 4%RH, but also the resulting error to be expected. We see that with the defined averaging,
674 random error is around 2% RH up to 5 km agl during nighttime and 1 km agl during daytime,
675 growing fast above.

676 Table 4. Statistics of observed differences for r_{H_2O} , T , and RH : experimental Mean Differences
677 (MD), Root-Mean Square Differences (RMSD), averaged over two different range bins, in the
678 low troposphere (1-2 km) and the free troposphere (5-6 km). Comparison to the “natural”
679 atmospheric variability between the lidar and RS sites as modelled by the ECMWF/IFS ERA5
680 reanalyses (difference over the considered period between grid points nearest to each of the two
681 sites), and to the theoretical root-mean-square error (RMSE) derived from the variance of the
682 RR signals. The grid points are located 8 km WNW of the lidar and 2 km S of the RS launching
683 station respectively, 18.3 km apart, and almost all RS trajectories below 6 km altitude are
684 contained within the same “pixel” of the ERA5 fields as the RS station.

	Range	Range resolution Δz	Model atmos. MD	Experimental MD (night/day)	Model atmos. RMSD	Theo. RMSE (night/day)	Experimental RMSD (night/day)
WVMR (g/kg)	1-2 km	84 m	-0.03	+0.06/-0.05	0.41	0.03/0.4	0.54/0.65
	5-6 km	168 m	<10 ⁻²	-0.07	0.11	0.04	0.15
Temperature (°C)	1-2 km	84 m	+0.15	+0.25/+0.1	0.33	0.4/0.7	0.6/1.0
	5-6 km	168 m	+0.05	+0.4	0.28	0.75	0.95
Relative humidity (%RH)	1-2 km	84 m	-0.23	+0.8/-0.5	6.37	1.7/5.5	6.5/10
	5-6 km	168 m	-0.70	-3.3	7.52	2.2	7

685

686 To support the above interpretation, in Table 4 we compare the experimental mean difference
687 and RMS difference plotted on Figure 13, averaged over two altitude ranges (low troposphere,
688 LT, 1 to 2 km, and free troposphere, FT, 5 to 6 km), to i) the natural variability of the atmosphere
689 between the radiosondes at Trappes and the lidar at LSCE, as modelled by ERA5 reanalyses of
690 the ECMWF/IFS weather model, ii) the expected random error given the noise level on the RR
691 signals. Nighttime and daytime values are indicated in the LT, only nighttime values in the FT.
692 We see that the experimentally observed values of RMSD are rather consistent with the
693 quadratic sum of the RMS variability of the atmospheric variables between Trappes and LSCE,
694 and of the noise-induced RMS error. The excess random difference is thus well explained by
695 the distance.

696 There is still a discrepancy with the mean difference of temperature below 1000 m between
697 daytime and nighttime however, probably due to the distance to the sounding station. Also, the
698 model used to approximate a regularized correction is still imperfect at such short ranges, and
699 introduce small errors when the necessary correction is large and fast-varying. We aim to
700 improve this in the future by launching radiosondes directly from the lidar site for calibration,
701 and by a better estimation the overlap ratios horizontally, for instance using a large folding
702 mirror instead of tilting the lidar, which induces varying mechanical constraints on the optics.

703 **5 Conclusion**

704 During the qualification of the rotational Raman channels for the WALI lidar of LSCE, with
705 the aim of providing profiles of relative humidity, we encountered important sources of bias
706 that are seldom described in the now abundant literature involving such systems. We
707 highlighted the predominant effects of the dependency of filter transmittance and detector
708 sensitivity upon angle of incidence and point of impact, respectively. Because the latter
709 parameters are directly proportional to field angle, they cause range-dependent biases on the
710 RR/VR signal ratios that are several times greater than the required accuracy of lidars for
711 temperature measurements (only 0.79% for 1°C here), less so for water vapor measurements.
712 We established that this effect cannot be suppressed by using fiber optics between the receiver
713 and polychromator, because scrambling of the lidar field of view does not happen radially in
714 the fiber. Mitigation efforts impose the careful alignment of each filter at normal incidence to
715 the input beam, and the verification of the spectral transmittance of each channel on a
716 spectrometer. The thermal stability of the polychromator is also of prime importance. Other
717 significant bias sources include electro-magnetic perturbations of signal baselines and PMT
718 gain variation, which must be mitigated. The impact of fiber optics fluorescence, and of the

719 measured laser linewidth or short-term wavelength drift were shown to be negligible in the
720 WALI system.

721 After a measurement of RR/VR channel ratios during horizontal shots, which showed the
722 significant impact of the above phenomena (up to 5% bias on ratios below 300m, ~1% higher),
723 we calibrated and de-biased the WALI measurements using radiosondes launched from the
724 nearby Trappes station of Météo-France. Between the de-clouded lidar measurements and the
725 radiosonde profiles, the remaining mean differences are small (below 0.1 g/kg on water vapor,
726 1°C on temperature) and RMS differences are consistent with the expected error from lidar
727 noise, calibration uncertainty, and horizontal inhomogeneities of the fields between the lidar
728 and radiosondes. On relative humidity we thus reach a goal of ~10%RH random error and
729 5%RH systematic error up to 9 km by night and 1.5 km by day, with 40 min time integration
730 and progressive vertical integration of 15 to 360 m at 10 km. The systematic error on RH is
731 dominated by bias on temperature, whereas the random error is dominated by noise on water
732 vapor measurements.

733 Thus exhaustively qualified, the WALI system may be applied in the near future to exercises
734 assimilating thermodynamic profiles in weather models, as is expected within the WaLiNeAs
735 (Water vapor Lidar Network Assimilation experiment) project (Flamant et al., 2021). The long-
736 term temporal evolution of Raman channel calibration, expected from various effects like
737 differential PMT aging or laser seeder drift, induces biases variable in time over the time-scale
738 of such a project (several months). This aspect is becoming a main focus as the community
739 works towards operational uses of weather Raman lidars (eg. Hicks-Jalali et al., 2020).

740 **Data and code availability**

741 The lidar data presented in this article, and information on code used for data processing, are
742 available upon request to Julien Totems at julien.totems@lsce.ipsl.fr. Radiosoundings from the
743 Tessereinc de Bort station (Trappes) were obtained at
744 https://donneespubliques.meteofrance.fr/?fond=produit&id_produit=97&id_rubrique=33,
745 courtesy of Météo France. ERA5 reanalyses of the ECMWF/IFS model were obtained at
746 <https://cds.climate.copernicus.eu/cdsapp#!/home> courtesy of the Copernicus Climate Change
747 Service (C3S).

748 **Author contribution**

749 JT designed, built and operated the new version of the WALI system, led the complementary
750 measurements on lidar components, processed the data, and wrote the article. PC
751 conceptualized the WALI system, acquired funding, and participated in structuring and
752 proofreading the paper. AB participated in the complementary measurements on lidar
753 components and in lidar/model comparisons, and proofread the paper.

754 **Competing interests**

755 The authors declare that they have no conflict of interest.

756 **Acknowledgements**

757 The authors thank Drs. Andreas Behrendt and Diego Lange for sharing component
758 specifications and for useful discussion. This work was funded by the Centre National d'Etudes
759 Spatiales (CNES), and by the Commissariat à l'Energie Atomique et aux Energies Alternatives
760 (CEA).

761 **References**

762 Adam, S., Behrendt, A., Schwitalla, T., Hammann, E. and Wulfmeyer, V.: First assimilation of
763 temperature lidar data into an NWP model: impact on the simulation of the temperature field,
764 inversion strength and PBL depth, *Q. J. R. Meteorol. Soc.*, 142(700), 2882–2896,
765 doi:10.1002/qj.2875, 2016.

766 Behrendt, A.: Temperature Measurements with Lidar, in *Lidar: Range-Resolved Optical*
767 *Remote Sensing of the Atmosphere*, vol. 102, edited by C. Weitkamp, pp. 273–306, Springer-
768 Verlag, New York., 2005.

769 Behrendt, A. and Reichardt, J.: Atmospheric temperature profiling in the presence of clouds
770 with a pure rotational Raman lidar by use of an interference-filter-based polychromator, *Appl.*
771 *Opt.*, 39(9), 1372, doi:10.1364/AO.39.001372, 2000.

772 Behrendt, A., Wulfmeyer, V., Hammann, E., Muppa, S. K. and Pal, S.: Profiles of second- to
773 fourth-order moments of turbulent temperature fluctuations in the convective boundary layer:
774 first measurements with rotational Raman lidar, *Atmos. Chem. Phys.*, 15(10), 5485–5500,
775 doi:10.5194/acp-15-5485-2015, 2015.

776 Buck, A. L.: New Equations for Computing Vapor Pressure and Enhancement Factor, *J. Appl.*
777 *Meteorol.*, 20(12), 1527–1532, doi:10.1175/1520-0450, 1981.

778 Chazette, P. and Totems, J.: Mini N₂-Raman Lidar onboard ultra-light aircraft for aerosol
779 measurements: Demonstration and extrapolation, *Remote Sens.*, 9(12), doi:10.3390/rs9121226,
780 2017.

781 Chazette, P., Marnas, F., Totems, J. and Shang, X.: Comparison of IASI water vapor retrieval
782 with H₂O-Raman lidar in the framework of the Mediterranean HyMeX and ChArMEx
783 programs, *Atmos. Chem. Phys.*, 14(18), 9583–9596, doi:10.5194/acp-14-9583-2014, 2014a.

784 Chazette, P., Marnas, F. and Totems, J.: The mobile Water vapor Aerosol Raman Lidar and its
785 implication in the framework of the HyMeX and ChArMEx programs: application to a dust
786 transport process, *Atmos. Meas. Tech.*, 7(6), 1629–1647, doi:10.5194/amt-7-1629-2014,
787 2014b.

788 Chazette, P., Raut, J.-C. and Totems, J.: Springtime aerosol load as observed from ground-
789 based and airborne lidars over northern Norway, *Atmos. Chem. Phys.*, 18(17), 13075–13095,
790 doi:10.5194/acp-18-13075-2018, 2018.

791 Chourdakis, G., Papayannis, A. and Porteneuve, J.: Analysis of the receiver response for a
792 noncoaxial lidar system with fiber-optic output, *Appl. Opt.*, 41(15), 2715,
793 doi:10.1364/AO.41.002715, 2002.

794 Cooney, J.: Measurement of Atmospheric Temperature Profiles by Raman Backscatter, *J. Appl.*
795 *Meteorol.*, 11(1), 108–112, doi:10.1175/1520-0450(1972)011<0108:MOATPB>2.0.CO;2,
796 1972.

797 Crevoisier, C., Clerbaux, C., Guidard, V., Phulpin, T., Armante, R., Barret, B., Camy-Peyret,
798 C., Chaboureau, J.-P., Coheur, P.-F., Crépeau, L., Dufour, G., Labonnote, L., Lavanant, L.,
799 Hadji-Lazaro, J., Herbin, H., Jacquinet-Husson, N., Payan, S., Péquignot, E., Pierangelo, C.,
800 Sellitto, P. and Stubenrauch, C.: Towards IASI-New Generation (IASI-NG): impact of
801 improved spectral resolution and radiometric noise on the retrieval of thermodynamic,
802 chemistry and climate variables, *Atmos. Meas. Tech.*, 7(12), 4367–4385, doi:10.5194/amt-7-
803 4367-2014, 2014.

804 Dinoev, T., Simeonov, V., Arshinov, Y., Bobrovnikov, S., Ristori, P., Calpini, B., Parlange, M.
805 and van den Bergh, H.: Raman Lidar for Meteorological Observations, RALMO – Part 1:
806 Instrument description, *Atmos. Meas. Tech.*, 6(5), 1329–1346, doi:10.5194/amt-6-1329-2013,
807 2013.

808 Flamant, C., Chazette, P., Caumont, O., Di Girolamo, P., Behrendt, A., Sicard, M., Totems, J.,
809 Lange, D., Fourrié, N., Brousseau, P., Augros, C., Baron, A., Cacciani, M., Comerón, A., De

810 Rosa, B., Ducrocq, V., Genau, P., Labatut, L., Muñoz-Porcar, C., Rodríguez-Gómez, A.,
811 Summa, D., Thundathil, R. and Wulfmeyer, V.: A network of water vapor Raman lidars for
812 improving heavy precipitation forecasting in southern France: introducing the WaLiNeAs
813 initiative, *Bull. Atmos. Sci. Technol.*, 2(1–4), 10, doi:10.1007/s42865-021-00037-6, 2021.

814 Fourrié, N., Nuret, M., Brousseau, P., Caumont, O., Doerenbecher, A., Wattrelot, E., Moll, P.,
815 Bénichou, H., Puech, D., Bock, O., Bosser, P., Chazette, P., Flamant, C., Di Girolamo, P.,
816 Richard, E. and Saïd, F.: The AROME-WMED reanalyses of the first special observation period
817 of the Hydrological cycle in the Mediterranean experiment (HyMeX), *Geosci. Model Dev.*,
818 12(7), 2657–2678, doi:10.5194/gmd-12-2657-2019, 2019.

819 Di Girolamo, P., Cacciani, M., Summa, D., Scoccione, A., De Rosa, B., Behrendt, A. and
820 Wulfmeyer, V.: Characterisation of boundary layer turbulent processes by the Raman lidar
821 BASIL in the frame of HD(CP)² Observational Prototype Experiment, *Atmos. Chem. Phys.*,
822 17(1), 745–767, doi:10.5194/acp-17-745-2017, 2017.

823 Hamamatsu: Characteristics of photomultiplier tubes, in *Photomultiplier tubes: basics and*
824 *applications*, third edition, Hamamatsu Photonics K.K. Electron Tube Division. [online]
825 Available from: [https://www.hamamatsu.com/resources/pdf/etd/PMT_handbook_v3aE-](https://www.hamamatsu.com/resources/pdf/etd/PMT_handbook_v3aE-Chapter4.pdf)
826 [Chapter4.pdf](https://www.hamamatsu.com/resources/pdf/etd/PMT_handbook_v3aE-Chapter4.pdf) (Accessed 29 April 2021), 2007.

827 Hammann, E., Behrendt, A., Le Mounier, F. and Wulfmeyer, V.: Temperature profiling of the
828 atmospheric boundary layer with rotational Raman lidar during the HD(CP)² Observational
829 Prototype Experiment, *Atmos. Chem. Phys.*, 15(5), 2867–2881, doi:10.5194/acp-15-2867-
830 2015, 2015.

831 Hayden Smith, W. and Smith, K. M.: A polarimetric spectral imager using acousto-optic
832 tunable filters, *Exp. Astron.*, 1(5), 329–343, doi:10.1007/BF00454329, 1990.

833 Hicks-Jalali, S., Sica, R. J., Martucci, G., Maillard Barras, E., Voirin, J. and Haefele, A.: A
834 Raman lidar tropospheric water vapour climatology and height-resolved trend analysis over
835 Payerne, Switzerland, *Atmos. Chem. Phys.*, 20(16), 9619–9640, doi:10.5194/acp-20-9619-
836 2020, 2020.

837 IPCC: *Climate Change 2013: The Physical Science Basis. Contribution of Working Group I to*
838 *the Fifth Assessment Report of the Intergovernmental Panel on Climate Change*, edited by T.
839 F. Stocker, D. Qin, G.-K. Plattner, M. Tigno, S. K. Allen, J. Boschung, A. Nauels, Y. Xia, V.
840 Bex, and P. M. Midgley, Cambridge University Press, Cambridge., 2013.

841 Kuze, H., Kinjo, H., Sakurada, Y. and Takeuchi, N.: Field-of-view dependence of lidar signals

842 by use of Newtonian and Cassegrainian telescopes, *Appl. Opt.*, 37(15), 3128,
843 doi:10.1364/AO.37.003128, 1998.

844 Lange, D., Behrendt, A. and Wulfmeyer, V.: Compact Operational Tropospheric Water Vapor
845 and Temperature Raman Lidar with Turbulence Resolution, *Geophys. Res. Lett.*, 46(24),
846 14844–14853, doi:10.1029/2019GL085774, 2019.

847 Martucci, G., Navas-Guzmán, F., Renaud, L., Romanens, G., Gamage, S. M., Hervo, M.,
848 Jeannet, P. and Haeferle, A.: Validation of pure rotational Raman temperature data from the
849 Raman Lidar for Meteorological Observations (RALMO) at Payerne, *Atmos. Meas. Tech.*,
850 14(2), 1333–1353, doi:10.5194/amt-14-1333-2021, 2021.

851 Navas-Guzmán, F., Martucci, G., Collaud Coen, M., Granados-Muñoz, M. J., Hervo, M.,
852 Sicard, M. and Haeferle, A.: Characterization of aerosol hygroscopicity using Raman lidar
853 measurements at the EARLINET station of Payerne, *Atmos. Chem. Phys.*, 19(18), 11651–
854 11668, doi:10.5194/acp-19-11651-2019, 2019.

855 Newsom, R. K., Turner, D. D., Mielke, B., Clayton, M., Ferrare, R. and Sivaraman, C.:
856 Simultaneous analog and photon counting detection for Raman lidar, *Appl. Opt.*, 48(20), 3903,
857 doi:10.1364/AO.48.003903, 2009.

858 Prunet, P., Thépaut, J.-N. and Cassé, V.: The information content of clear sky IASI radiances
859 and their potential for numerical weather prediction, *Q. J. R. Meteorol. Soc.*, 124(545), 211–
860 241, doi:10.1002/qj.49712454510, 1998.

861 Sherlock, V., Garnier, A., Hauchecorne, A. and Keckhut, P.: Implementation and Validation of
862 a Raman Lidar Measurement of Middle and Upper Tropospheric Water Vapor, *Appl. Opt.*,
863 38(27), 5838, doi:10.1364/AO.38.005838, 1999.

864 Sicard, M., Chazette, P., Pelon, J., Won, J. G. and Yoon, S.-C.: Variational method for the
865 retrieval of the optical thickness and the backscatter coefficient from multiangle lidar profiles,
866 *Appl. Opt.*, 41(3), 493, doi:10.1364/AO.41.000493, 2002.

867 Simeonov, V., Larcheveque, G., Quaglia, P., van den Bergh, H. and Calpini, B.: Influence of
868 the photomultiplier tube spatial uniformity on lidar signals, *Appl. Opt.*, 38(24), 5186,
869 doi:10.1364/AO.38.005186, 1999.

870 Totems, J. and Chazette, P.: Calibration of a water vapour Raman lidar with a kite-based
871 humidity sensor, *Atmos. Meas. Tech.*, 9(3), 1083–1094, doi:10.5194/amt-9-1083-2016, 2016.

872 Totems, J., Chazette, P. and Raut, J.-C.: Accuracy of current Arctic springtime water vapour

873 estimates, assessed by Raman lidar, *Q. J. R. Meteorol. Soc.*, 145(720), doi:10.1002/qj.3492,
874 2019.

875 Vaughan, G., Wareing, D. P., Pepler, S. J., Thomas, L. and Mitev, V.: Atmospheric temperature
876 measurements made by rotational Raman scattering, *Appl. Opt.*, 32(15), 2758,
877 doi:10.1364/AO.32.002758, 1993.

878 Wandinger, U. and Ansmann, A.: Experimental determination of the lidar overlap profile with
879 Raman lidar, *Appl. Opt.*, 41(3), 511, doi:10.1364/AO.41.000511, 2002.

880 Weng, M., Yi, F., Liu, F., Zhang, Y. and Pan, X.: Single-line-extracted pure rotational Raman
881 lidar to measure atmospheric temperature and aerosol profiles, *Opt. Express*, 26(21), 27555,
882 doi:10.1364/OE.26.027555, 2018.

883 Whiteman, D. N.: Examination of the traditional Raman lidar technique I Evaluating the
884 temperature-dependent lidar equations, *Appl. Opt.*, 42(15), 2571, doi:10.1364/AO.42.002571,
885 2003.

886 Whiteman, D. N., Melfi, S. and Ferrare, R.: Raman lidar system for the measurement of water
887 vapor and aerosols in the Earth's atmosphere, *Appl. Opt.*, 31(16), 3068–82,
888 doi:10.1364/AO.31.003068, 1992.

889 Whiteman, D. N., Cadirola, M., Venable, D., Calhoun, M., Miloshevich, L., Vermeesch, K.,
890 Twigg, L., Dirisu, A., Hurst, D., Hall, E., Jordan, A. and Vömel, H.: Correction technique for
891 Raman water vapor lidar signal-dependent bias and suitability for water vapor trend monitoring
892 in the upper troposphere, *Atmos. Meas. Tech.*, 5(11), 2893–2916, doi:10.5194/amt-5-2893-
893 2012, 2012.

894 WMO: WMO Oscar : List of all requirements, [online] Available from: [https://www.wmo-](https://www.wmo-sat.info/oscar/requirements)
895 [sat.info/oscar/requirements](https://www.wmo-sat.info/oscar/requirements) (Accessed 28 April 2021), 2017.

896 Wulfmeyer, V., Hardesty, M. R., Turner, D. D., Behrendt, A., Cadeddu, M. P., Di Girolamo,
897 P., Schlüssel, P., Baelen, J. Van and Zus, F.: A review of the remote sensing of lower
898 tropospheric thermodynamic profiles and its indispensable role for the understanding and the
899 simulation of water and energy cycles, *Rev. Geophys.*, 819–895, doi:10.1002/2014RG000476,
900 2015.

901